https://doi.org/10.5194/egusphere-2026-2890
Preprint. Discussion started: 16 July 2026


# Tsunami modeling at lake-scale using non-linear shallow water equations

Jana C. Schierjott[1], Paola Bacigaluppi[1], and David F. Vetsch[1]
[1]VAW, ETH Zürich, Hönggerbergring 26, 8093 Zürich
**Correspondence:** Jana C. Schierjott (schierjott@vaw.baug.ethz.ch)

**Abstract.** The steep slopes and shores along lakes and reservoirs in mountainous regions, specifically with glacial history such as the Alps, Alaska or the Himalaya, are prone to terrestrial and subaqueous mass movements. Particularly, increasing temperature due to climate change may affect the stability of mountain slopes because of thawing permafrost and retreating glaciers. Moreover, particular sediment-mechanical properties promote subaqueous mass movements in regions which have experienced glaciation. The occurring mass movements may lead to the generation of a tsunami-like wave when interacting with the water body of a lake or reservoir causing considerable damage to infrastructure and endangering human lives. A prominent example was documented on Lake Lucerne in central Switzerland in 1601. A series of subaqueous landslides following an earthquake led to a tsunami with wave heights of up to 4 m, which flooded parts of the city of Lucerne. Other examples in Switzerland and abroad show that the danger of a lake tsunami is very real. A detailed risk assessment is therefore crucial for mitigation or prevention of such hazard. Current state-of-the-art tools for tsunami modeling are typically used in ocean settings. In this study we evaluate whether models based on hydrostatic and non-hydrostatic non-linear shallow water equations also produce reliable results in lake settings, i.e. for smaller water depth and shorter propagation distance. We perform benchmark tests and compare results to experimental data in order to assess the applicability of hydrostatic versus non-hydrostatic non-linear shallow water equation solvers for tsunami modeling at lake-scale.

## 1 Introduction

Earthquake-triggered or spontaneous terrestrial or subaqueous mass movements into confined water bodies can result in tsunamis leading to severe impacts on coastal population and infrastructure (Hoffmann and Reicherter, 2016; Lee and Jones, 2014; Jiang and LeBlond, 1992; Tappin, 2017). Compared to ocean-tsunamis that typically arrive on wide beaches, wave propagation and run-up in narrow basins such as lakes is more complex due to complicated bathymetry and topography making modeling a very important tool in hazard assessment and mitigation. On the one hand, waves may very quickly loose their energy due to reflections and negative interference but on the other hand, in certain cases, exactly the narrow confined geometry can lead to amplification and a huge run-up (Didenkulova and Pelinovsky, 2011). Miller (1960) investigated a tsunami wave triggered by terrestrial mass movements in Lituya Bay, USA in 1958, where the wave eroded trees up to 365 m inland and 33 m above lake level. A similar event occurred at Chehalis Lake, Canada, in 2007 (Roberts et al., 2013; Wang et al., 2015), with documented and simulated run-up heights of around 37 m at the opposite shore. The resulting tsunami wave traveled

https://doi.org/10.5194/egusphere-2026-2890
Preprint. Discussion started: 16 July 2026


through the whole lake (7.5 km) and propagated downstream the river for up to 15 km. Luckily, the campsite at the lake was not occupied so no fatalities occurred. The waves historically documented for the ca. 6200 BC Storegga event (Harbitz, 1992; Løvholt et al., 2005) and recorded for the 1998 Papua New Guinea event (Heinrich et al., 2001; Synolakis et al., 2002) most likely resulted from subaqueous mass movements triggered by earthquakes. In the latter, run-up heights were recorded to be around 10 m and severe damage to infrastructure and 2200 fatalities were recorded (Heinrich et al., 2001). Just recently, a new prominent example has drawn attention: a large rockfall triggered a tsunami wave in a Greenlandic fjord which continued to slosh through the fjord for several days (Svennevig et al., 2024). This extreme example shows that wave energy sometimes cannot easily escape from lakes. The possible reflections and interferences of waves in lakes also mean that the first wave does not necessarily have to be the largest (Couston et al., 2015), thus requiring extended computational power for modeling and risk assessment.

In the future, the risk for lake tsunamis is likely to rise due to climate change. For example, heavier rainfalls may destabilize slopes around lakes or trigger subaqueous mass movements at river deltas because of stronger sediment input and higher discharge. Furthermore, glacier and permafrost retreat can destabilize rock faces around reservoirs (McColl, 2012; Gariano and Guzzetti, 2016; Hock et al., 2019; Wolken et al., 2021; Patton et al., 2021; Svennevig et al., 2025; Jacquemart et al., 2024). On top of that, the worldwide growing population and increasing tourism justifies the need for a better understanding of the impact of lake tsunamis on coastal communities (Rafliana et al., 2022; Fathianpour et al., 2023).

There are various numerical studies on lake-scale tsunamis (Harbitz et al., 2014; Hilbe and Anselmetti, 2015; Kremer et al., 2015; Strupler et al., 2018; Svennevig et al., 2024). Most of these studies tend to use one specific method or solver based either on the hydrostatic or on the non-hydrostatic nonlinear shallow water equations (SWE) and compare it to previously applied similar methods or to natural or laboratory examples. For example Harbitz et al. (2014) used two different non hydrostatic SWE codes (GloBouss and DpWaves), Hilbe and Anselmetti (2015) as well as Strupler et al. (2018) coupled mass movement modeling (MassMov2D) with a hydrostatic SWE solver (GeoClaw), both Nigg et al. (2021), Kremer et al. (2015) each applied a hydrostatic SWE solver and compared modeling outcomes to natural data, and Ruffini et al. (2019) used a wide range of geometries in laboratory and numerical experiments but only used one non-hydrostatic SWE solver (SWASH). One of the few studies that compare different approaches was performed by St-Germain et al. (2014) who compared results from a smoothed particle hydrodynamics method (DualSPHysics), non-hydrostatic SWE (SWASH) and laboratory experiments. Løvholt et al. (2015) performed a rigorous comparison of different solvers in terms of results and computational characteristics but hydrostatic SWE solver played only a very minor role. Because Harbitz et al. (2014) reported difficulties in correctly modeling run-up and inundation as well as numerical instabilities when applying non-hydrostatic SWE solvers in the fjord setting, Løvholt et al. (2015) also used a combination of several solvers (GloBouss, Coulwave, MOST).

As both, the hydrostatic as well as the non-hydrostatic SWE approach, have their advantages and disadvantages, hybrid approaches that couple both models have become an important strategy for coastal inundation and wave-breaking applications (**?**Kazolea and Ricchiuto, 2018; Bacigaluppi et al., 2019). However, coupling of models, similarly to the use of non-hydrostatic SWE solvers, is associated with greater time expenditure which oftentimes is a crucial factor in hazard assessment and mitigation.

https://doi.org/10.5194/egusphere-2026-2890
Preprint. Discussion started: 16 July 2026


In this study we evaluate the applicability of two solvers based on hydrostatic and non-hydrostatic SWE to the setting of lake tsunamis. We apply these two solvers to a wave channel whose scale is based on Lake Lucerne, Switzerland, with depths ranging between 25 m and 200 m, and a maximum length of 6.4 km. The goal is to gain a better understanding of how the two different approaches influence wave height, propagation, and, in particular, run-up. We further validate the applicability of the hydrostatic SWE solver BASEMENT for lake-scale tsunamis by comparing laboratory and numerical experiments with the aim of providing a sufficiently accurate, and at the same time fast tool for lake tsunami modeling in hazard assessment.

## 2 Governing Mathematical Equations

In the following, we introduce the applicability range of two typically used mathematical concepts for tsunami modeling: the hydrostatic (h) and non-hydrostatic (nh) SWEs. We recall the equations considering a Cartesian reference system $(x, y, z)$ in which the $z$ axis is vertical and the $x-y$ plane is horizontal.

### 2.1 Hydrostatic SWE models (h-SWE)

To simulate tsunami waves, oftentimes hydrostatic SWEs (e.g. LeVeque et al. (2011)) are applied. These are derived from the Navier-Stokes (NS) equations under the assumption of negligible vertical velocities and thus hydrostatic pressure distribution over the flow depth (shallow water region). While these simplifications reduce computational costs, they lead to inaccurate results when applied in the wrong context. h-SWE models are usually well-suited for describing flows in near-shore areas, particularly for (i) waves with large wavelengths ($\lambda \gg 20 h_{ref}$), and (ii) waves with relatively small amplitudes $A$ ($A \ll h_{ref}$). These models work particularly well for representing wave fronts due to their natural dissipation mechanisms, which prevent numerical oscillations during run-up or breaking wave fronts. On the other hand, h-SWE models cannot capture the dispersive effects of waves very well. However, in a relatively shallow and small lake setting, this is likely of secondary importance. For a detailed review of h-SWE models, the reader may refer to (Brocchini and Dodd, 2008).

The system of governing equations for the h-SWE model (e.g. Ambrosi (1995)) can be written as

$$\frac{\partial h}{\partial t} + \frac{\partial q_x}{\partial x} + \frac{\partial q_y}{\partial y} = S_h, \tag{1}$$

$$\frac{\partial q_x}{\partial t} + \frac{\partial}{\partial x}\left(\frac{q_x^2}{h} + \frac{1}{2}gh^2\right) + \frac{\partial}{\partial y}\left(\frac{q_x q_y}{h}\right) = gh\left(S_{bx} + S_{fx}\right), \tag{2}$$

$$\frac{\partial q_y}{\partial t} + \frac{\partial}{\partial x}\left(\frac{q_y q_x}{h}\right) + \frac{\partial}{\partial y}\left(\frac{q_y^2}{h} + \frac{1}{2}gh^2\right) = gh\left(S_{by} + S_{fy}\right) \tag{3}$$

where $h(x,y,t) = h_{ref} + \eta(x,y,t)$ is the water depth, constituting from the sum of the still water reference depth $h_{ref}$ and possible water surface elevation due to waves in terms of $\eta(x,y,t)$, as shown in the sketch in figure 2. $g$ is acceleration of gravity, $u$ is the depth-averaged velocity in $x$ and $v$ the same in $y$ direction, $q_x$ is the discharge per unit width in $x$ ($q_y$ in $y$) direction.

The bed slope source terms are defined as $S_{bx} = \frac{\partial b}{\partial x}$ and $S_{by} = \frac{\partial b}{\partial y}$, accordingly, with $b(x,y,t)$ the topography or bathymetry. $S_h$ is the lateral inflow/outflow discharge per unit width, while $S_{fx}$ contains the friction terms in $x$ ($S_{fy}$ in $y$) direction.

https://doi.org/10.5194/egusphere-2026-2890
Preprint. Discussion started: 16 July 2026


Adopting a quadratic friction law, the friction term is proportional to the square of the depth-averaged velocity and can be written as $S_{fx} = \frac{u|\boldsymbol{u}|}{gc_f^2 h}$ and, accordingly, $S_{fy} = \frac{v|\boldsymbol{u}|}{gc_f^2 h}$, where $|\boldsymbol{u}| = \sqrt{u^2+v^2}$ is the magnitude of the velocity vector and $c_f$ is the dimensionless friction coefficient.

### 2.2 Non-hydrostatic SWE models (nh-SWE)

h-SWE models are not suitable for representing wave motion in deep or transitional regions. Using the h-SWE formulation for relatively short waves in deep water can result in excessive dissipation. Therefore, non-hydrostatic models that include dispersive terms are necessary to capture wave spreading and different wave speeds. One of the first of nh-SWE models uses the so-called Boussinesq equations, proposed by Boussinesq in 1872, followed by Peregrine's wave equations in 1967. Various authors derived similar or improved the existing equations, such as Nwogu (1993) whose model considers the velocity at a certain depth, or Madsen et al. (1991); Madsen and Sørensen (1992), who extended Peregrine's equations to intermediate depths by introducing higher order-terms. Other models further take into account the non-linearity of the wave, e.g. the equations derived by Kim et al. (2001); Lannes and Bonneton (2009), that contain a hyperbolic part as well as Boussinesq-typical dispersive terms. For a detailed review of the nh-SWE models, the reader may refer to Brocchini (2013).

The following described set of nh-SWE are a simplification of the equations derived by Schäffer and Madsen (1995). Originally, the equations included a higher-order term of $\mathcal{O}(\mu^4)$ in order to optimize linear dispersion properties. The below presented equations are in 1D-form, following the approach in Kim et al. (2017), but without friction:

$$\frac{\partial h}{\partial t} + \frac{\partial q_x}{\partial x} = 0, \tag{4}$$

$$(1-\mathcal{D})\frac{\partial q_x}{\partial t} + \frac{\partial}{\partial x}\left(\frac{q_x^2}{h} + \frac{1}{2}gh^2\right) - ghS_{bx} = -\Psi(x,t), \tag{5}$$

$$\left(B+\frac{1}{2}\right)h_{ref}^2\left[\frac{\partial^2}{\partial x^2}\left(\frac{\partial}{\partial x}\left(\frac{q_x^2}{h}\right) + gh\frac{\partial \eta}{\partial x}\right)\right] - \frac{1}{6}h_{ref}^3\left[\frac{\partial^2}{\partial x^2}\left(\frac{\partial}{\partial x}\left(\frac{q_x^2}{hh_{ref}}\right) + \frac{gh}{h_{ref}}\frac{\partial \eta}{\partial x}\right)\right] = \Psi(x,t), \tag{6}$$

$$\left(B+\frac{1}{2}\right)h_{ref}^2\left(\frac{\partial^2 w}{\partial x^2}\right) - \frac{1}{6}h_{ref}^3\frac{\partial^2}{\partial x^2}\left(\frac{w}{h_{ref}}\right) = \mathcal{D}(w), \tag{7}$$

with $\mathcal{D}$ being the differential operator containing spatial derivatives for a dummy variable $w(x,t)$, $\Psi(x,t)$ as a source term and $B$ as a dispersion parameter (Kim et al., 2017).

## 3 Numerical Approach

For the present study, three different software were considered, i.e. BASEMENT, GeoClaw and BoussClaw. The underlying numerical approximation for all three software is the finite volume method. Following the works of Vetsch et al. (2019), Berger et al. (2011) and Kim et al. (2017), we briefly recall the main aspects of the numerical methods of each tested software.

BASEMENT (Vetsch et al., 2019) and GeoClaw (GC) (Berger et al., 2011) share the same mathematical model, namely the h-SWEs.

https://doi.org/10.5194/egusphere-2026-2890
Preprint. Discussion started: 16 July 2026


### 3.1 BASEMENT

BASEMENT (BAsic-Simulation-EnvironMENT) was originally designed for 2D-river hydro- and morphodynamic simulations in alpine and sub-alpine regions. It can simulate steady and unsteady flow conditions as well as sediment erosion and deposition. BASEMENT makes use of the finite volume approach to solve the governing mathematical equations on an unstructured grid with arbitrary geometry. The possibility of multi-core CPU, GPU and hybrid CPU-GPU accelerated simulations allows for high performance computing, along with its optimized design to guarantee the stability and robustness of the numerical methods.

The hydraulic fluxes are calculated at the element edges according to the initial states of the left and right cells using the Harten-Lax-van Leer Contact (HLLC) Riemann solver (Toro et al. (1994)).

Time integration follows an explicit first order Euler scheme. Numerical stability is assured by choosing the time step $\Delta t$ for time integration according to the Courant-Friedrichs-Lewy (CFL) number, defined in the 2D-context as $CFL = \frac{1}{r_i}\left(\sqrt{u^2+v^2}+c\right)\Delta t$, where $r_i$ is the radius of the inscribed circle that defines the element center, while $u$, $v$ are the corresponding velocities of the element and $c = \sqrt{gh}$. The applied HLLC solver is stable for $0 < CFL \leq 1$. Subsequently, the hydraulic state variables i.e. cell-centered quantities are updated and, finally, the source terms are calculated.

### 3.2 GeoClaw

GeoClaw is a well-established software based on the Clawpack platform (Team) and is widely used in the context of h-SWE tsunami modeling (e.g. Hilbe and Anselmetti (2015); Strupler et al. (2018); Montoya and Lynett (2016)). It is part of the Clawpack solver (Team), a class of high-resolution finite volume methods that considers cell averages of the solution over each cell, composed by logically rectangular grids. The applied method is of Godunov-type, solving a Riemann problem at each cell edge with the possibility to add correction terms for a second order-accuracy in smooth regions of the flow. In GeoClaw, the difference of the flux normal to the cell interface can be split into propagating waves after the inclusion of the bathymetric source term (so-called "f-wave formulation" (George, 2008)), which improves the stability and the overall accuracy. Another advantage of Geoclaw is its ability to work with adaptive mesh refinement which can keep the computational efficiency high, while guaranteeing an overall good representation of the approximated solution.

### 3.3 BoussClaw

The BoussClaw solver is based on and an extension of the GeoClaw solver with additional dispersion terms. It is written for the Boussinesq-type equations derived by Schäffer and Madsen (1995), i.e. accounting for possible frequency dispersion-related issues. This software relies on the modeling equations presented in equation 7. The h-SWE part of the mathematical system is approximated via a finite volume technique, while the additional terms, comprising higher order derivatives, are discretized via the finite difference method. BoussClaw first solves the h-SWE model with the f-wave method (like GeoClaw), subsequently adding the friction term and then solves the system

$$(1-\mathcal{D})\frac{\partial q_x}{\partial t} = -\Psi. \tag{8}$$

https://doi.org/10.5194/egusphere-2026-2890
Preprint. Discussion started: 16 July 2026


For the spatial discretization, a second order-centered scheme was adopted, along a four stage Runge-Kutta method for the time integration, as described in detail in the work of Kim et al. (2017).

## 4 Study-Scenario and Experimental setup

### 4.1 Parameter range

For the numerical setup, we chose Lake Lucerne in Switzerland as a reference lake. Lake Lucerne is a peri-alpine lake, partly surrounded by steep slopes, prone to subaqueous or terrestrial mass movements, similar to fjords (e.g. Harbitz et al. (2014)). Waves can travel between 5 km and 10 km across various basins (fig. 1). The absolute water depth of Lake Lucerne ranges from 25 m to 214 m.

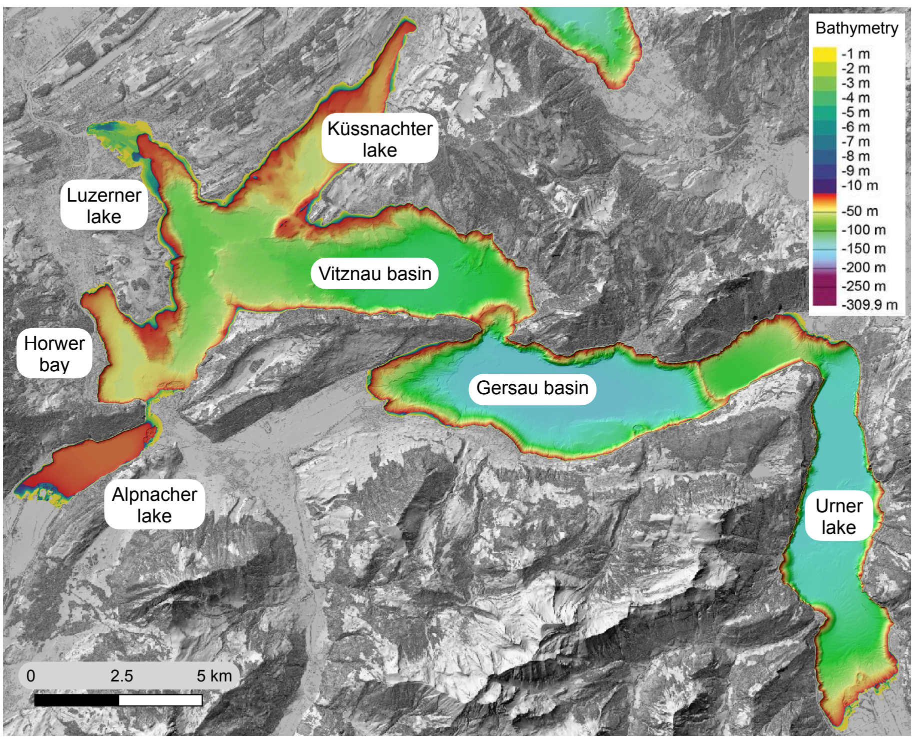


**Figure 1.** Topography and bathymetry of Lake Lucerne showing all its different basins. Data source: SwissTopo.

There is historical evidence for tsunami waves in Lake Lucerne triggered by subaqueous mass movements (Nigg et al., 2021; Watts et al., 2005; Strupler et al., 2020a; Hilbe and Anselmetti, 2015; Schnellmann et al., 2002; Siegenthaler and Sturm, 1991). According to previous studies, wave amplitudes $A$ ranged from 0.1 m to a maximum of 8.0 m. Using a still water reference depth $h_{ref}$ = between 25 m and 200 m, the relative wave amplitude ($\varepsilon = A/h_{ref}$) ranges between $0.0025 - 0.32$, and relative wave lengths $L_w/h_{ref}$ between 12.8 and 114.7.

https://doi.org/10.5194/egusphere-2026-2890
Preprint. Discussion started: 16 July 2026


The investigated parameter range in the numerical experiments is based on the above mentioned findings and derived values (table 1). All numerical experiments were computed without friction and a constant CFL number of $0.8$.

| $h_{ref}$ $[m]$ | | $A$ $[m]$ | | | | | |
|---|---|---|---|---|---|---|---|
| | | 0.1 | 0.5 | 1.0 | 2.0 | 4.0 | 8.0 |
| 25 | $\varepsilon$ | 0.04 | 0.02 | 0.04 | 0.08 | 0.16 | 0.32 |
| | $\frac{L_w}{h_{ref}}$ | 114.7 | 51.3 | 36.3 | 25.7 | 18.1 | 12.8 |
| 50 | $\varepsilon$ | 0.002 | 0.01 | 0.02 | 0.04 | 0.08 | 0.16 |
| | $\frac{L_w}{h_{ref}}$ | 162.2 | 72.6 | 51.3 | 26.3 | 25.7 | 18.1 |
| 100 | $\varepsilon$ | 0.001 | 0.005 | 0.01 | 0.02 | 0.04 | 0.08 |
| | $\frac{L_w}{h_{ref}}$ | 229.4 | 102.6 | 72.6 | 51.3 | 36.3 | 25.7 |
| 200 | $\varepsilon$ | - | 0.0025 | 0.005 | 0.01 | 0.02 | 0.04 |
| | $\frac{L_w}{h_{ref}}$ | - | 145.1 | 102.6 | 72.6 | 51.3 | 36.3 |

**Table 1.** Relative wave height $\varepsilon = \frac{A}{h_{ref}}$ and relative wave length $\frac{L_w}{h_{ref}}$ for different amplitudes ($A$) and water depths ($h_{ref}$).

## 4.2 Wave type

Generally, solitary waves have been widely used in ocean-tsunami modeling (Madsen et al., 2008a). One of the reasons is the existing general solution to the solitary wave equation with only two unknowns (Madsen et al., 2008a). Furthermore, Hammack Jr and Raichlen (1972); Hammack (1973); Segur (1973) and other authors showed that a sudden positive or negative change in the water level (e.g. due to a landslide, earthquake) at constant water depth results in a solitary wave. Goring and Raichlen (1978) and Yeh et al. (1994) found that after a long propagation period, the tsunami wave corresponds to the shape of a solitary wave. However, Madsen et al. (2008a) demonstrated that on geophysical scales (e.g. average ocean depth and average tsunami height in ocean), this is not likely to happen: The relation $x/href \approx 0.062\varepsilon^{\frac{-3}{2}}$ derived by Madsen et al. (2008b) leads to unrealistically large threshold values for a solitary wave to form, based on average ocean values (4000 m depth, 1 m wave height). At the lake scale, the threshold values are still (too) large ($x =$775 m), but much closer to what is realistically possible (e.g. 100 m depth, 4 m wave height). This is due to the different origin of the waves that are mass-movement induced (lead to relatively large wave heights) in case of lake tsunamis. According to several authors (Madsen et al., 2008a; Madsen and Schaeffer, 2010; Tadepalli and Synolakis, 1994; Chan and Liu, 2012; Liang et al., 2013; Qu et al., 2017) a solitary wave underestimates the energy, or run-up respectively, compared to the use of a N-wave model (e.g. three $sech2(*)$ wave profiles or similar concepts) and hence the reach of the overland flow and the force the tsunami wave carries. However, on the other hand, Fuchs (2013) found that the use of a solitary wave will rather lead to a conservative run-up result due to the absence of a wave trough and a resulting larger potential energy. Taking the wide range of literature into account, it is important to acknowledge that solitary waves are neither perfect nor the only option for modeling tsunami waves, and that using a solitary wave or any other type of wave has its advantages and disadvantages.

https://doi.org/10.5194/egusphere-2026-2890
Preprint. Discussion started: 16 July 2026


We compute the boundary condition for BASEMENT ($\eta$ as water surface elevation in space and time, $u$ as velocity in space and time) for the solitary wave following Lo et al. (2013); Madsen et al. (2008a):

$$\eta(x,t) = A\mathrm{sech}^2\left(\kappa\left[x - t\sqrt{g\,(h_{ref} + A)}\right]\right), \text{ with } \kappa = \sqrt{\frac{3A}{4h_{ref}^2\,(A + h_{ref})}}, \tag{9}$$

$$u(x,t) = \frac{\eta(x,t)\sqrt{g\,(A + h_{ref})}}{h_{ref} + \eta(x,t)}, \tag{10}$$

where $A$ is the maximum wave amplitude and $g$ gravitational acceleration. GeoClaw and BoussClaw both also use a solitary wave to model tsunami waves. This allows for a straight-forward comparison in-between software and with experimental data.

## 4.3 Model Setup

The numerical model setup is twofold: one set of numerical experiments is performed in a wave channel with lake-scale, the second and third set follow the setup by Fuchs (2013). For both setups we apply the following notation: Wave amplitude is always denoted by $A$, the wave length by $L_w$, the total possible propagation distance by $S$, the water surface elevation in space and time by $\eta$, the run-up height by $r$, the height of the shore by $w$, the distance between water surface elevation and shore height by $Z_f$, and the height of the overland flow by $d$.

### 4.3.1 Lake-scale model: Wave Channel

The numerical tests investigating accuracy of the different software are performed in a wave channel with open boundary on the downstream side (fig. 2). In the numerical model, the solitary wave starts at the left boundary of the modeling domain and propagates over the whole length $S$ =6.4 km towards the opposite side. The still water reference depth $h_{ref}$ is varied in this scenario between 25 and 200 m. To assess the error during propagation we measure the wave amplitude and period at nine artificial gauges (0.0, 0.05, 0.1, 0.2, 0.4, 0.8, 1.6, 3.2 and 6.4 km) with respect to the starting point/bottom of the wave in GeoClaw and BoussClaw, and the first cell of the domain after the input boundary of BASEMENT. These locations are denoted by ‘G#’ followed by an increasing number from 1-9 (fig. 2).

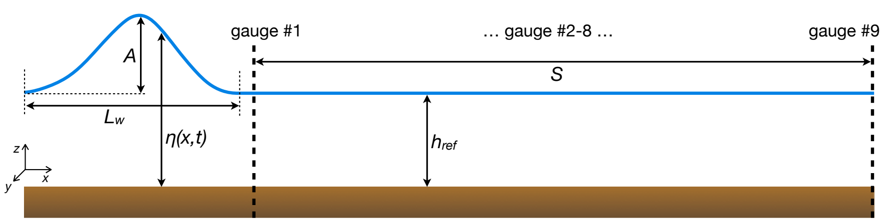


**Figure 2.** Setup 1: Lake-scale wave channel.

Since we apply three different codes with different characteristics, each model setup differs slightly. BASEMENT utilizes an unstructured grid in x-y direction given by triangles; GeoClaw is based on a mesh consisting of rectangles. In order to

https://doi.org/10.5194/egusphere-2026-2890
Preprint. Discussion started: 16 July 2026


have comparable cell sizes, we follow Yu et al. (2012), and apply the relation $A_Q = \frac{4}{3} A_T$, with $A_Q$=4 $m^2$ and $A_T$=3 $m^2$ for the cell areas of the quadrangles and triangles, respectively. The quadrangles are square-shaped with 2 m-long edges. A mesh sensitivity test showed that there is not a convincing gain in accuracy by using a finer mesh (Appendix A). BoussClaw was validated for 1D simulations with benchmarks in Kim et al. (2017). The chosen constant parameters in the x-y space in the 2D-simulations allow us to compare the results from all three codes.

The wave generation differs between BASEMENT and GeoClaw/BoussClaw. In GeoClaw/BoussClaw the solution is imposed on the spatial domain (x,y)-coordinates as initial condition, while in BASEMENT the wave is generated via a boundary condition. Therefore, for each simulation the water surface displacement over time at $1.5L_w$ (the base of the solitary wave) in GeoClaw is measured and used as input boundary conditions for the respective BASEMENT simulation.

#### 4.3.2 Experimental-scale models

The second and third set of numerical experiments follows the setup by Fuchs (2013) who conducted experiments in a 11.0 m-long, 0.5 m-wide, and 1.0 m-deep wave channel. The estimated roughness coefficients in the experimental channel vary between 0.0–0.003 mm for glass and 0.01–0.1 mm for steel. The experimental data by Fuchs (2013) was measured optically via photographs using a single lens reflex camera with 16 mm wide-angle lens and acquisition frequencies of 5 Hz. The measurement error of the camera is estimated to 3 mm. The maximum water surface elevation on the shore was acquired every 0.005 s during the simulation. Details about the experiments can be found in the publication (Fuchs, 2013). The cell area in the second set of numerical models is 0.00002 $m^2$.

**Wave Run-up**

The solitary wave starts at the left boundary of the wave channel with still water reference depth $h_{ref}$ and propagates towards the opposite side 3. At the end of the channel an upward-angling slope with angle $\beta$ is located to simulate run-up. Following Fuchs (2013), the propagation distance is set to $S = 25h_{ref}$ m. To avoid boundary reflections, the total modeling domain is set to $2h_{ref} + 2L_w$. The bottom of the slope starts at $S = 20w$ for an inclination of$\tan\beta = \frac{1}{5}$, to $S = 22.5w$ for an inclination of $\tan\beta = \frac{1}{2.5}$, and to $S = 23.5w$ for an inclination of $\tan\beta = \frac{1}{1.5}$. The shore height is set to $w$=0.25 m for all experiments.

We evaluate the maximum run-up height $r$ with regard to different still water reference depths ($h_{ref}$ =0.2 m and 0.1 m.), initial wave amplitudes ($A = 8, 18, 19, 27, 38, 58$ mm), underwater slopes ($\tan\beta = \frac{1}{5}$, $\frac{1}{2.5}$, $\frac{1}{1.5}$), and bed roughness ($k_b = 0.2$, 0.5, 1 mm). The bed roughness is part of the friction coefficient $c_f$ according to Chézy, s.t. $c_f = 5.75\log\left(12\frac{h}{k_b}\right)$ if $h > k_b$, else $c_f = 5.75\log(12)$. The ratio of the initial wave amplitude to still water reference depth is depicted as $\varepsilon$ on the y-axis of the shown figures.

https://doi.org/10.5194/egusphere-2026-2890
Preprint. Discussion started: 16 July 2026


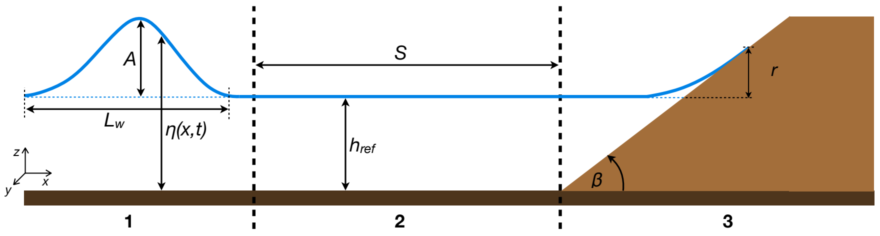


**Figure 3.** Setup 2: Wave channel with wave run-up based on the experimental setup by (Fuchs, 2013).

**Overland flow**

235 For the study of the overland flow, the setup is very similar to the study of the run-up height 4. The solitary wave starts at the left end of the wave channel with still water reference depth $h_{ref}$ and travels over a distance $S$, where an upward-facing slope starts. The slope starts ends at transition point $x_{tr}$ where the initially dry overland area begins. The overland extends for a distance of $12.5h_{ref}$, measured from $x_{tr}$. Six gauges are set: The first one is located at $x_{tr}$; every $2w$ there is the next one. The gauges are set at the exact same locations as in the physical experiment performed by Fuchs (2013).

240 We consider two different underwater slopes $\tan\beta = \frac{1}{5}$ and $\tan\beta = \frac{1}{1.5}$, three different still water reference depths of 0.2, 0.22 and 0.24 m and several amplitudes for each $h_{ref}$ so that the relative amplitude $\varepsilon$ takes values between 0.1 and 0.3. The freebord distance $z_f = w - h_{ref}$ varies between 0.01 and 0.05 m, with $w$=0.25 m.

- $h_{ref} = 0.24$ m: wave amplitudes are $A = 24.4$, 48.5 and 71.5 mm corresponding to $\varepsilon$ =0.1, 0.2 and 0.3.
- $h_{ref} = 0.22$ m: wave amplitudes are $A = 22.3$, 44.6 and 66.3 mm corresponding to $\varepsilon$ =0.1, 0.2 and 0.3.
- 245 $h_{ref} = 0.2$: wave amplitudes are $A = 40.2$ and 60.0 mm corresponding to $\varepsilon$ =0.2 and 0,3.

This leads us to two investigated scenarios using various values for $h_{ref}$ and $A$ for the following two set-ups:

1. When the slope is set to $\tan\beta = \frac{1}{1.5}$, the distance $S = 11.5w$. The slope ends at $x_{tr} = 1.5w$.
2. When the slope is set to $\tan\beta = \frac{1}{5}$, the distance $S = 2.4w$. The slope ends at $x_{tr} = 5w$.

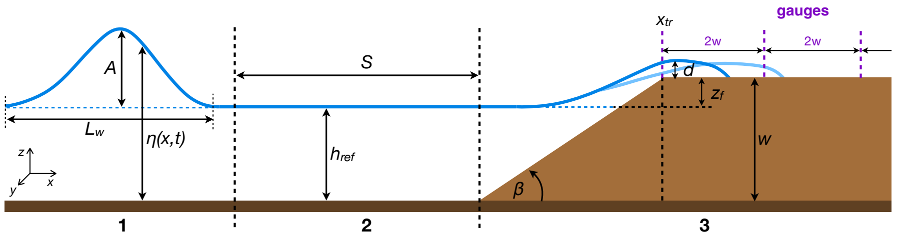


**Figure 4.** Setup 3: Wave channel with overland flow based on the experimental setup by (Fuchs, 2013).

https://doi.org/10.5194/egusphere-2026-2890
Preprint. Discussion started: 16 July 2026


## 5 Results Part 1: Numerical model comparisons in a straight channel

### 5.1 Comparison of order of accuracy

First, we compare solutions of BASEMENT, GeoClaw (both h-SWE solvers) and BoussClaw (nh-SWE solver) for a first and second order accuracy of the numerical method. We start a wave in a straight wave channel (fig. 2) and compare the wave shape and height at several gauges to the initial wave amplitude-input.

#### 5.1.1 1st order accuracy

We start off by providing a qualitative assessment of how the wave shape and amplitude change after 6.4 km of wave propagation compared to the initial input. The results are summarized in table 2. A clear overall trend is visible: the larger the initial wave amplitude in smaller still water depths the more likely are changes in wave amplitude and shape. Small waves do not seem to change their shape and amplitude much, particularly for larger still water depths.

| $A\ [m]$ | $h_{ref}\ [m]$ | | | |
|---|---|---|---|---|
| | 25 | 50 | 100 | 200 |
| 0.1 | X | X | X | X |
| 0.5 | ✓ | X | X | X |
| 1.0 | ✓ | (✓) | X | X |
| 2.0 | ✓ | (✓) | (✓) | X |
| 4.0 | ✓ | ✓ | (✓) | (✓) |
| 8.0 | ✓ | ✓ | (✓) | (✓) |

**Table 2.** Overview of visible "✓", somewhat visible "(✓)" and non-visible "X" differences in wave heights and shape after 6.4 km of propagation on an undisturbed bathymetry.

In the following we have a more detailed look at how the wave shape changes over the course of the model run and in-between the different solvers. Figure 5 shows the water surface displacement versus time at gauge #9 for a wave with the same initial amplitude of $A = 4$ m (a) and b)) but different initial still water depths (a) ($h_{ref} = 100$ m) and b) ($h_{ref} = 25$ m). Panel c) displays the resulting water surface displacement for a wave with initial amplitude of $A = 0.5$ m and $h_{ref} = 25$ m, panel d) a zoom on the peak of the wave with initial conditions of again $A = 0.5$ m and but the largest still water reference depth $h_{ref} = 200$ m.

In the tests with the smaller still water reference depth of $h_{ref} = 25$ m (fig. 5 a), c)) the wave shape and height deviate much more from the reference wave than in tests with larger still water reference depth, particularly when using the h-SWE solvers and for a large $\varepsilon$ (fig. 5 a)).

https://doi.org/10.5194/egusphere-2026-2890
Preprint. Discussion started: 16 July 2026


The solution of the nh-SWE solver shows better agreement with the original wave input regarding the wave shape. The wave height and width differs from the reference case as well. In the test cases plotted in panel b) and d) all waves almost perfectly keep their height. However, the solutions of both h-SWE solvers show a small deviation in wave shape from the reference wave while the solution of the nh-SWE solver overlaps with the initial wave profile (fig. 5 b)) and neither deviates in size nor in shape from the reference wave. The scenario with the smallest $\varepsilon$ shows barely any difference in-between solvers and also in-between reference case and numerical solutions (5 d)).

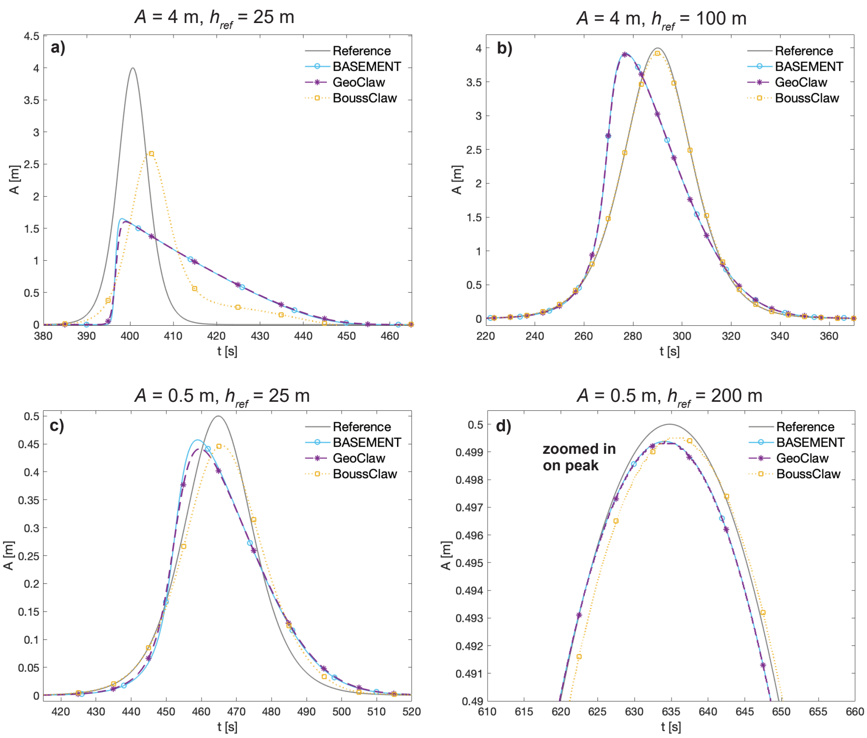


**Figure 5.** Comparison of BASEMENT, GeoClaw and BoussClaw results at gauge #9 against the initial wave (input reference) for 1st order accuracy.

The found deviations from the reference wave, specifically the solutions by the h-SWE solvers, solely occur at gauge #9, located at a distance of 6.4 km from the initial wave input. At prior gauges, the wave shape and height produced by the h-SWE solvers are much more similar to the solution by the nh-SWE solver (fig. 6). Both h-SWE solver consistently produce the same results, over the whole propagation distance.

In order to quantitatively asses how much the wave shape and amplitude changes with propagation distance, we investigate the variation of the wave amplitudes in percentage at the gauges located at distances $s$ with respect to the initial amplitude measured at gauge #1, formulated as $A^{t,s}_{max} = \frac{max_t A_s}{max_t A_{ref}} \cdot 100 - 100$. We display these results for four different amplitudes:

https://doi.org/10.5194/egusphere-2026-2890
Preprint. Discussion started: 16 July 2026


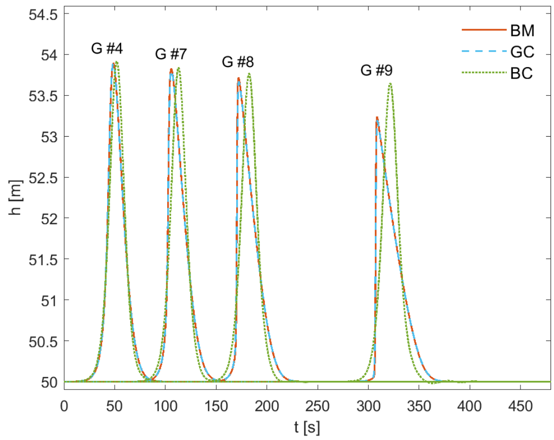


**Figure 6.** Benchmark for $A = 4$ m and $h_{ref} = 50$ m. Comparison between BASEMENT (BM), GeoClaw (GC) and BoussClaw (BC) at gauges located at 0.2 km (#4), 1.6 km (#7), 3.2 km (#8) and 6.4 km (#9).

$A = 0.5$, 2, 4 and 8 m (fig. 7). We notice that for still water depths of $h_{ref} = 100$ and 200 m the distortion and dissipation of the wave is negligible, independent of the initial wave amplitude. For a still water depth of 50 m and small wave amplitudes (such as 0.5 m and 2 m) the distortion and dissipation is also negligible. However, when initial wave amplitudes are larger (e.g. here 4 m and 8 m) and smaller still water reference depths of 50 m, the wave shape and amplitude changes, particularly in solutions by the h-SWE solvers.

When the still water depth is even smaller (25 m), we observe that all solvers produce a wave distorted from the reference wave. In most scenarios, the nh-SWE solver leads to waves with the smallest errors regarding wave shape and amplitude. In the scenario with the smallest still water depth and the smallest amplitude (fig. 7 a)) the solution with BASEMENT is the most accurate. There is a very good overall agreement between both h-SWE solvers BASEMENT and GeoClaw, with a slightly higher accuracy of solutions by BASEMENT for smaller amplitudes (fig. 7). Errors of the 1st order for $A^{t,s}_{max}$ and $\Delta t_s = \frac{\Delta t_{\text{ref}}}{\Delta t_{ref}} \times 100 - 100$ are included in appendix C.

### 5.1.2 2nd order accuracy

To determine any possible advantages by applying a higher order of accuracy of the numerical method, we investigate the scenarios presented in table 2 with a second order of accuracy and a monotonized central limiter for both, the GeoClaw and BoussClaw software. The numerical wave channel set-up is the same as in the previous section.

Figure 8 shows the difference between the second and the first order accuracy of the variation of the wave amplitudes in percentage ($\Delta A^{t,s}_{max}$) for a wave with an amplitude of $A = 2$ m (left) and $A = 8$ m (right) at different still water levels $h_{ref}$ and gauge distances $s$. The error of the maximum amplitude is computed as before ($A^{t,s}_{max} = \frac{max_t A_s}{max_t A_{ref}} \cdot 100 - 100$).

https://doi.org/10.5194/egusphere-2026-2890
Preprint. Discussion started: 16 July 2026


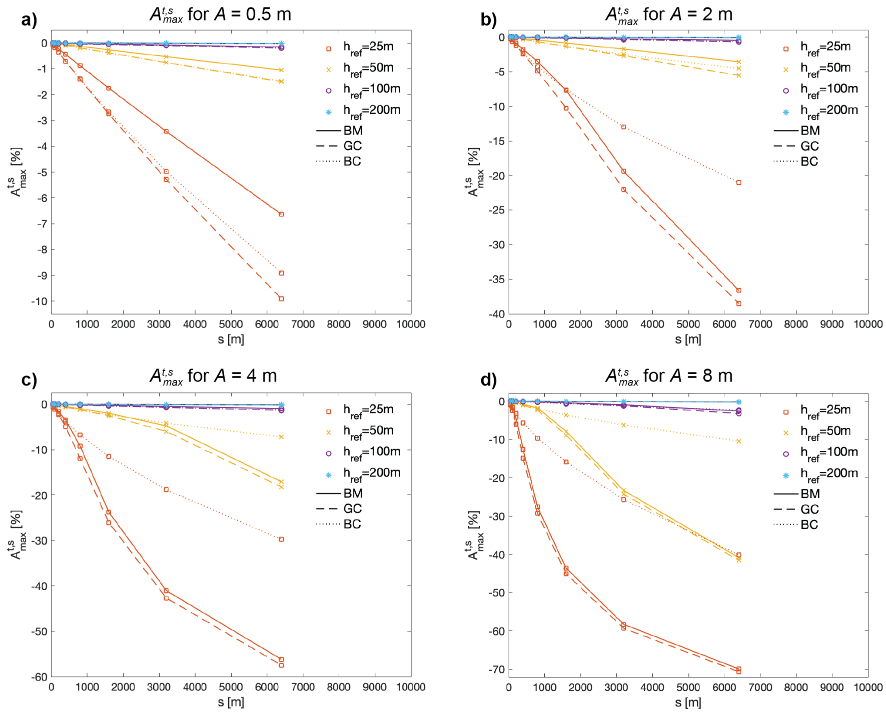


**Figure 7.** Variation in percentage of the maximum amplitude at the gauge located at the distance $s$ w.r.t. the initial amplitude measured at gauge #1. Comparison between BASEMENT, (BM), GeoClaw (GC) and BoussClaw (BC) for different water depths and four initial wave amplitudes.

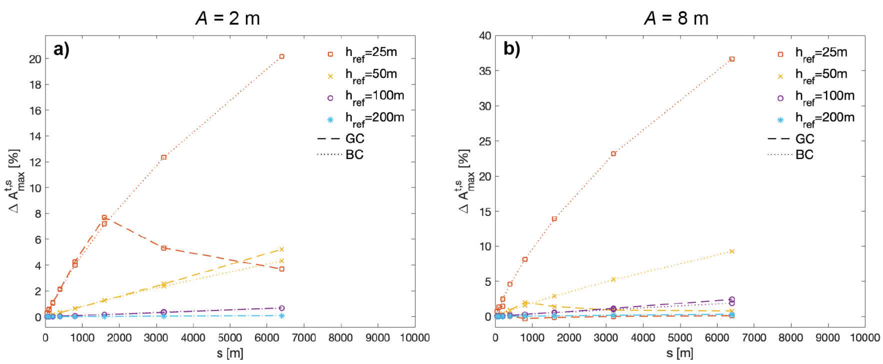


**Figure 8.** Difference between 1st and 2nd order accuracy of the variation of the wave amplitudes in percentage ($\Delta A^{t,s}_{max}$) at several gauges w.r.t. the initial amplitude measured at gauge #1. Comparison between GeoClaw (GC) and BoussClaw (BC) for different water depths and wave amplitudes (a) $A = 2$ m) and b) $A = 8$ m).

In the scenarios with larger $h_{ref}$ (100 and 200 m) (fig. 8), there exist almost no differences in variation of the wave amplitude between first and second order of accuracy. In these cases, a second order of accuracy does not add any valuable advantage.

https://doi.org/10.5194/egusphere-2026-2890
Preprint. Discussion started: 16 July 2026


However, for $h_{ref} = 50$ m and $A = 2$ m we observe a linear increase of accuracy with respect to the propagation distance for both h-SWE solvers; similarly for the nh-SWE solver, but with $A = 8$ m. In the case of $h_{ref} = 25$ m and both amplitudes, a remarkable increase in accuracy can be reached for the nh-SWE solver. The improvement reaches up to 20% for the smaller amplitude and more than 35% for $A = 8$ m (at a propagation distance of 6.4 km). Errors of the 2nd order for $A^{t,s}_{max}$ and $\Delta t_s = \frac{\Delta t_{\mathrm{ref}}}{\Delta t_{ref}} \times 100 - 100$ are included in appendix D.

## 6 Results Part 2: Wave run-up and overland flow

In this section, we evaluate how bed roughness and slope inclination affect (i) the run-up height of the wave and (ii) the overland flow. We compare outcomes of a numerical study using h-SWE solver BASEMENT to laboratory experiments by Fuchs (2013).

### 6.1 Wave Run-up

**Impact of bed roughness**

Figure 9 shows the relative wave amplitudes $\varepsilon$ plotted against the measured maximum run-up height $r$. The general trend in both, the numerical and experimental data shows an increase in run-up height for larger relative wave amplitudes and/or larger $h_{ref}$. There is a good agreement between the experimental and numerical data.

On closer inspection, as the value of $\varepsilon$ increases towards 0.3, the experimental and numerical results diverge more. For the larger still water reference depth of 0.2 m, the difference between experimental and numerical results varies between 21.2% and 23.2%. For the smaller still water reference depth of 0.1 m, the difference between experimental and numerical results is smaller (15.7% to 21.6%).

The different values of bed roughnesses tested in the numerical simulations do not significantly affect the run-up height. For the smaller $h_{ref}$ of 0.1 m, the run-up height is the same for all tested bed roughnesses. For the larger $h_{ref}$ of 0.2 m, the run-up height is slightly smaller for larger bed roughnesses, but a lot less variable than the results of the laboratory experiments.

**Impact of slope**

Next, we investigate the run-up on a slope with different inclinations $\tan\beta = \frac{1}{5} \approx 11°$, $\frac{1}{2.5} \approx 22°$ and $\frac{1}{1.5} \approx 34°$.

The numerical results show a complex behavior and no clear trend (fig.10). As a first general observation, the run-up height always increases with larger relative wave amplitude, for all slope inclinations. This is expected from the experimental and numerical results discussed above. Second, we notice that for the steepest slope inclination the run-up height is the lowest.

Comparing the numerical results to the experimental results, we see that for smaller slope inclinations, BASEMENT results overestimate the run-up height. For the largest slope inclination $\tan\beta = \frac{1}{5}$ and $\varepsilon = 0.3$, BASEMENT clearly underestimates the run-up height, whereas for smaller $\varepsilon$ and the same slope inclination the run-up height matches the experimental results closely.

https://doi.org/10.5194/egusphere-2026-2890
Preprint. Discussion started: 16 July 2026


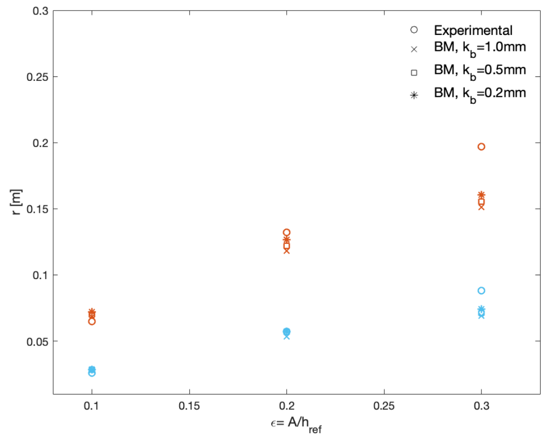


**Figure 9.** Maximum run-up height (r) on a slope with different bed roughness against relative wave amplitude $\varepsilon$. Comparison between experimental data from Fuchs (2013) and the numerical approximation of BASEMENT for $h_{ref} = 0.2$ m (red) and $h_{ref} = 0.1$ m (blue).

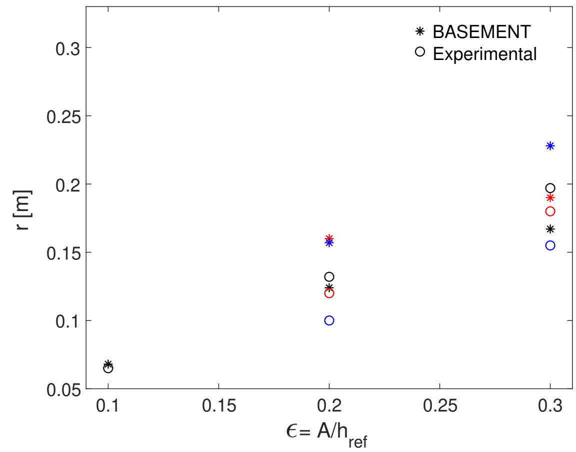


**Figure 10.** Run-up (r) at constant water depth for different slopes: $\tan\beta = \frac{1}{5}$ (black), $\tan\beta = \frac{1}{2.5}$ (red) and $\tan\beta = \frac{1}{1.5}$ (blue). Comparison between the experimental data from Fuchs (2013) and the numerical approximation of BASEMENT.

## 6.2 Overland flow

335 **Impact of bed roughness**

In this section we investigate the sensitivity of the recorded flow depth towards bed roughness. We compare the numerical results to experimental data by Fuchs (2013). We use different bed roughness with height $k_b$ ranging between 0 and 2 mm and

https://doi.org/10.5194/egusphere-2026-2890
Preprint. Discussion started: 16 July 2026


a still water reference depth of $h_{ref} = 0.2$ m. Figure 11 displays the results for relative wave amplitude $\varepsilon = 0.2$ on the left panel, and those for $\varepsilon = 0.3$ on the right panel. Generally, the numerical and experimental results agree for both relative wave amplitudes at all gauges. Looking at the results in more detail, it can be seen that in general all numerical experiments with $k_b$= 0.0 mm show the largest difference between experimental and numerical data. This is somewhat surprising, since the laboratory experiments have a shore made of PVC, which has a very low roughness. Therefore, one would expect the best fit for the lowest $k_b$ in the numerical experiments. The largest variation in flow depth measured in the numerical experiments themselves is at 0.5 m (the first gauge actually located on the overland area). This can be explained by the effect of roughness on how easily the water can spread across the overland. Another observation is that overall bed roughness is slightly less important at higher relative wave amplitudes than at lower relative amplitudes.

Taking into account an experimental measurement error from the ultrasonic device of around 3 mm, all numerical approximations provide a very well fitting result for almost all $k_b$ for both $\varepsilon$.

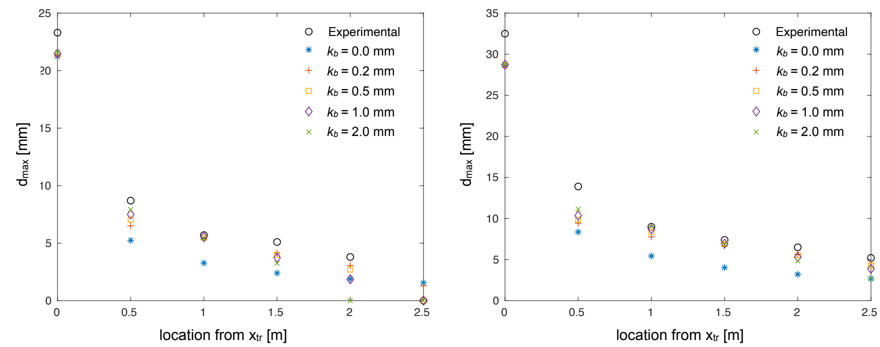


**Figure 11.** Flow depth at the transition point $x_{tr}$ and at several gauges set every $2w$ to the left of it. Comparison between the experimental data from Fuchs (2013) and the numerical approximation of BASEMENT for different bed roughness $k_b$. On the left panel, $\varepsilon = 0.2$, on the right $\varepsilon = 0.3$.

**Impact of slope**

Here we analyze the sensitivity of the recorded flow depth with regard to the slope of the shore. We again compare the numerical results to experimental data by Fuchs (2013). Note that only limited experimental data is available for $\varepsilon = 0.1$. Overall, there is very good agreement between the numerical and experimental results for all cases. The small deviations between the data may be due to measurement errors and/or inaccuracy of the measuring device in the laboratory. In both the numerical and experimental results, several trends can be observed. The larger the distance from the transition point $x_{tr}$, the less the relative wave amplitude matters for the flow depth. Furthermore, a smaller $h_{ref}$ a slope inclination leads to smaller flow depths. While at the transition point the flow depth differs greatly between the different slope inclinations (about 15 mm), the flow depths start to converge shortly after, implying that the slope does not necessarily affect the flow depth, especially at greater distances from the shore.

https://doi.org/10.5194/egusphere-2026-2890
Preprint. Discussion started: 16 July 2026


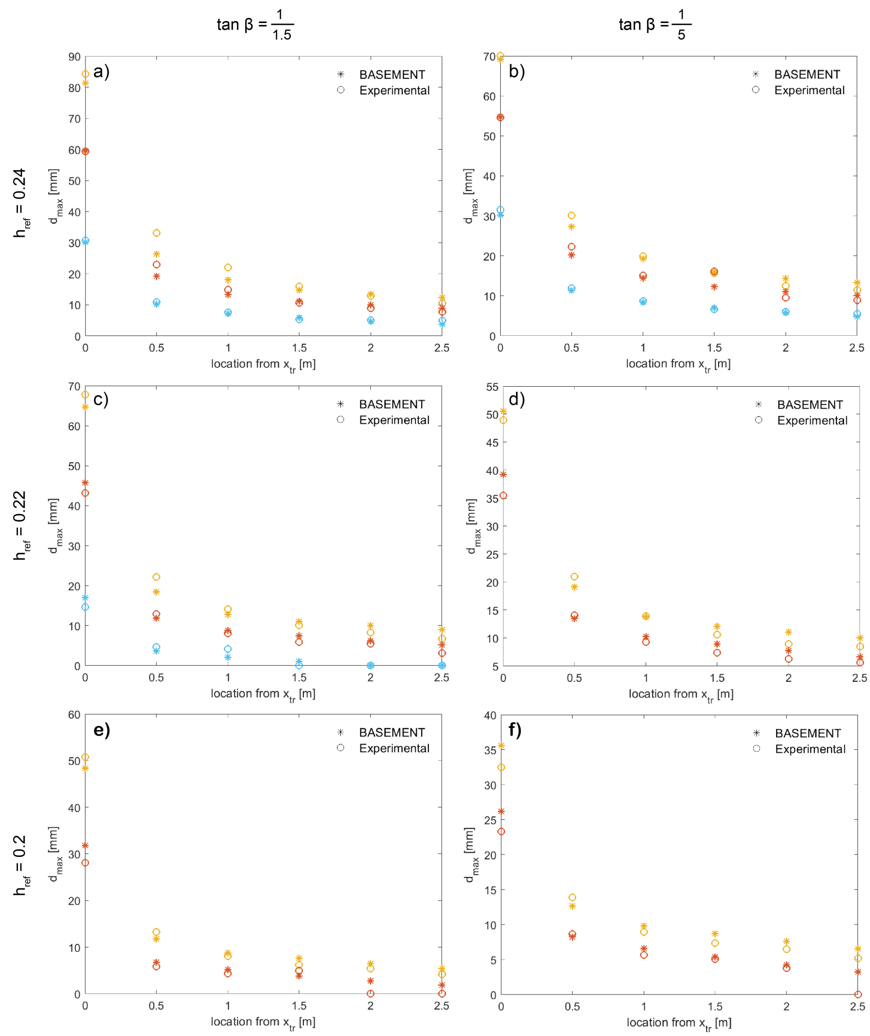


**Figure 12.** Flow depth at the transition point $x_{tr}$ and at several gauges located every $2w$ left of it. Comparison between the experimental data from Fuchs (2013) and the numerical approximation of BASEMENT for various combinations of slope and still water reference depth. Color coded are the values of the relative wave amplitudes: $\varepsilon = 0.1$ (blue), $\varepsilon = 0.2$ (red) and $\varepsilon = 0.3$ (yellow).

## 7 Discussion

### 7.1 Wave propagation in a straight channel

The comparison of three different software (one nh-SWE, two h-SWE solver) to model wave propagation reveals important findings for natural hazard protection. In the particular setting of a straight channel, the use of h-SWE solvers is for most scenarios an evenly good option as the use of an nh-SWE solver. For smaller wave amplitudes, both h-SWE solvers accurately model wave propagation, shape and size, even over longer distances. This finding is particularly important when discussing

https://doi.org/10.5194/egusphere-2026-2890
Preprint. Discussion started: 16 July 2026


flood protection and mitigation due to waves in smaller volumes of water, such as lakes. The results reveal that the use of a more computationally expensive nh-SWE solver is not necessarily necessary in order to receive accurate wave shapes and sizes when traveling distances are not excessively large. In lake settings, usually the traveling distance of waves is usually relatively short (e.g. find lake sizes).

Furthermore, an h-SWE solver can even be the better choice because wave breaking and inundation can be captured more accurately (discussed in section 7.2.1 and 7.2.2 in more detail). Regarding the choice of a certain h-SWE solver, there are almost no differences in results between GeoClaw, an established solver for wave modeling, and BASEMENT, a tool originally developed for river modeling.

When the ratio $\epsilon$ of amplitude to still water depth increases due to larger wave amplitude or smaller $h_{ref}$, wave shape and size deviate more from the reference wave using an h-SWE solver than when employing a nh-SWE solver. This behavior is expected as wave dispersion, interaction, steepening and shoaling cannot be accurately modeled by regular h-SWE solvers. Hence, the choice of solver depends to some extent on the overall goal: to accurately model the wave shape and dispersion, particularly over long distances or in a regime leaning towards intermediate-water, an nh-SWE (such as BoussClaw) solver might be preferable over an h-solver, to receive accurate results for overland flow and run-up in a relatively short computational time, an h-SWE solver might be the preferred option.

## 7.2 Comparison numerical and laboratory experiments

We compare the numerical outcomes with laboratory experiments of Fuchs (2013) to understand whether using an h-SWE solver for tsunami modeling at lake-scale not only compares well with applying an nh-SWE solver, but also captures inherent features of laboratory experiments.

### 7.2.1 Run-up

Numerical and laboratory results match well for almost all tested run-up height scenarios. In one test case (largest slope inclination $= 34°$ and largest relative wave amplitude $\varepsilon = 0.3$) BASEMENT underestimates the run-up height compared to the laboratory data by Fuchs (2013) whose results also slightly underestimate the run-up height when compared to data by for example Hall et al. (1953). It seems as if generally for such a steep slope the variation in run-up height is greater than for smaller inclinations and smaller relative wave amplitudes. One explanation for the tendency of the numerical simulations to underestimate the run-up height might be the inaccurate representation of dissipation and dispersion of waves relative to laboratory experiments. However, the inaccuracy in the discussed scenario should not be of great concern regarding the validity of the numerical model as there is a general variability in run-up height even in-between laboratory experiments. Further, the chosen angle of 34° is generally on the upper end of natural materials making up lake slopes: 34° is the angle of repose for dry sand (Beakawi Al-Hashemi and Baghabra Al-Amoudi, 2018, and references therein). Clay can have a higher angle of repose (25° - 40°), whereas gravel a lower one (25° - 30°). Water can influence these values to a high extent as well (Beakawi Al-Hashemi and Baghabra Al-Amoudi, 2018). One could argue that in nature a slope with such a large inclination would rather be unstable and collapse, and therefore does not represent a typical lake slope. It has been observed that even though slopes in

https://doi.org/10.5194/egusphere-2026-2890
Preprint. Discussion started: 16 July 2026


lakes can vary greatly between 5° and 60°, most of them are on the flatter side (< 20°) (Strasser et al., 2011; Strupler et al., 2017). Strupler et al. (2020b) for example classified all slopes with an angle < 20° as unstable. Following this, wave run-up modeled with BASEMENT would rather lead to a more conservative result, since for smaller slope inclinations BASEMENT tends to overestimate the run-up height.

Overall, the agreement between experimental and numerical results is very good. The bed roughness does not significantly affect the run-up. There is a tendency to underestimate the run-up for large slope inclinations and large $\varepsilon$ and to overestimate the run-up height for small slope inclinations for all $\varepsilon$. The latter seems more likely in natural lake environments which leads to a conservative result in risk assessment.

#### 7.2.2 Overland flow

The analysis of the effect of bed roughness on overland flow shows that the numerical and experimental results are in good agreement for both relative wave amplitudes at all gauges. The largest difference between numerical and laboratory results can be seen when the bed roughness $k_b$=0.0 mm in the numerical experiments, although the laboratory experiments use PVC (with extremely low bed roughness) as the shore and bank material. Further away from the transition point, the flow depths differ less between the numerical experiments themselves and also compared with the laboratory results. Overall, the numerical experiments lie within the measurement error of the laboratory experiments.

The slope inclination affects the depth of the overland flow close to the transition point, while at distance, the flow depths start to converge. This is noticeable in numerical and laboratory experiments alike, implying that the slope does not necessarily affect the flow depth to a large extent. With respect to overland flow, BASEMENT does not show any shortcomings. The numerical and laboratory results are in agreement both in trends and in absolute values. The numerical results are within the error of the measuring device in cases where the laboratory and numerical results differ. The observations and conclusions drawn from the numerical results agree with the results of Fuchs (2013).

The inherent feature of h-SWE solvers is that inundation, run-up and overland flow can be captured well. This, we could verify by comparing modeling results of BASEMENT to experimental results by Fuchs (2013). As was stated by e.g. Lynett (2022), the dissipation of energy due to breaking at the shore does not significantly impact the general run-up and overland flow (velocities). Hence, the applicability of h-SWE is given, particularly in lake settings where distances are generally shorter and the emphasis is on risk assessment and hazard mitigation, e.g. run-up and overland flow matter more than a perfectly accurate wave shape.

In a next step, in-depth analysis of different numerical modeling solutions of propagating waves in a wave basin could be performed to understand how the three dimensions of the basin affect dispersion, dissipation and attenuation of the wave and how numerical solutions compare to laboratory results.

https://doi.org/10.5194/egusphere-2026-2890
Preprint. Discussion started: 16 July 2026


## 8 Conclusions

In this study we compare solutions from h-SWE (GeoClaw, BASEMENT) and nh-SWE (BoussClaw) solvers in order to evaluate the applicability of h-SWE solvers in wave modeling, particularly tsunami modeling at lake-scale. We find that h-SWE solvers can be employed in most scenarios instead of a computationally more expensive nh-SWE solver. The most limiting factor for the usage of an h-SWE solver is a large ratio of wave amplitude to still water depth (e.g. $\varepsilon \geq 0.08$). The second limiting factor is a very large propagation distance, in which the nh-SWE solver better keeps the wave shape and amplitude compared to the tested h-SWE solvers, BASEMENT and GeoClaw. However, this mostly matters when wave amplitude and shape are of high relevance for the investigation rather than the run-up.

To confirm the applicability of the h-SWE solver we compare results of numerical experiments performed with the h-SWE solver BASEMENT to laboratory experiments by Fuchs (2013); again in a wave channel setup. Slope inclination and bed roughness are tested for their influence on overland flow and run-up. The results of laboratory and numerical experiments match overall very well. As was demonstrated in the laboratory experiments, the numerical experiments show that the bed roughness does not significantly affect the run-up. Also the overall impact of bed roughness on overland flow is small; the distance from the transition point plays a much larger role. Indeed, the comparison between laboratory and numerical experiments even shows that a large $\varepsilon$ discussed in the paragraph above is not hindering when investigating overland flow and run-up, even though the wave shape and amplitude may differ from the input wave.

Overall, our findings reveal that faster h-SWE solvers can produce results as accurate as those obtained using more computationally expensive nh-SWE solvers under most conditions. Specifically in most lake settings, the two solving methods can be used interchangeably. Attention must be paid when the propagation distance is greater than 6 km and when the wave shape itself is relevant. When overland flow and run-up height are the most important factors, as is typically the case in risk assessments and hazard mitigation, an h-SWE solver provides a fast, accurate solution in a lake-scale setting.

*Code availability.* The hydro- and morphodynamic simulation tool BASEMENT is freely available here: https://basement.ethz.ch.

https://doi.org/10.5194/egusphere-2026-2890
Preprint. Discussion started: 16 July 2026


450 # Appendix A: Mesh sensitivity and performance

## A1 Performance and speed

The sequential (single core) implementation of the code BASEMENT is run on an Intel Xeon Gold 5218 CPU with 16 cores and 2.3 GHz clock speed. Regarding the CUDA simulations, we test three different Nvidia GPU cards: a low-end Ge-Force GTX1070Ti and two high-end cards, Tesla K20c (Kepler architecture) and Tesla P100 (Pascal architecture). More details can
455 be found in table A1.

| GPU card | Cores | Base clock [GHz] | Memory [GB] | Bandwidth [GB/s] | Launch Price [USD] (year) |
|---|---|---|---|---|---|
| Ge-Force GTX1070Ti | 2432 | 1.68 | 8 | 256 | 399 (2017) |
| Tesla K20c | 2496 | 0.706 | 5 | 208.0 | 3200 (2012) |
| Tesla P100 | 3584 | 1.19 | 12 | 549.1 | 4600 (2016) |

**Table A1.** Specifications of the GPU cards.

Figure A1 shows the speedup (b) against the number of cells in the computational domain obtained for different types of waves (linear and non-linear), for different GPU architectures compared to a single-core CPU simulation. The excellent performance underlines the importance of a highly optimized computational tool in order to allow a fast calculation of possible tsunami scenarios.

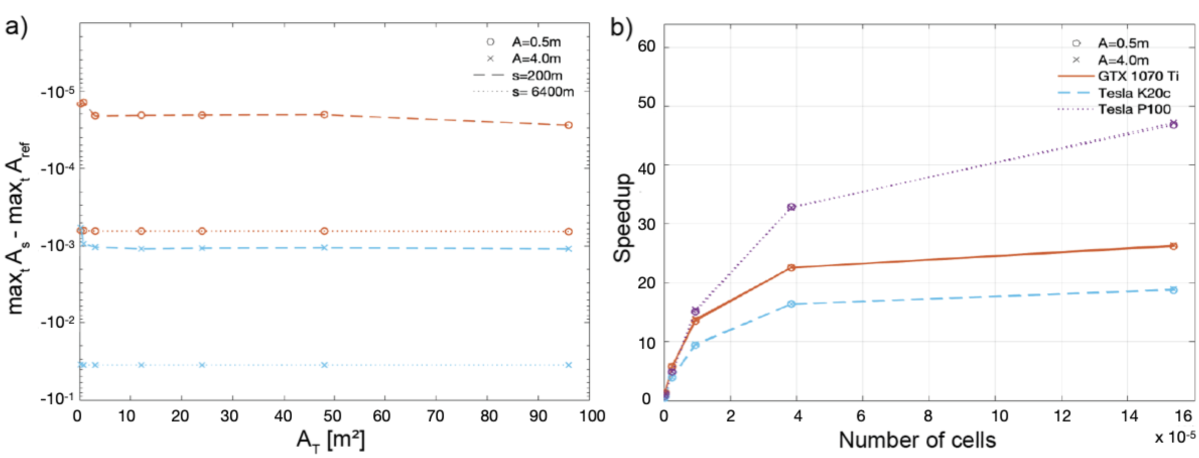


**Figure A1.** a) Maximum water height error for different mesh refinements. b) Speedup on different GPU architectures with respect to a CPU single-core.

https://doi.org/10.5194/egusphere-2026-2890
Preprint. Discussion started: 16 July 2026


460 ### A1.1 Errors mesh sensitivity

Table A2 shows the percentage of the maximum water height error, checked at two different distances, i.e. 200 m and 6.4 km of propagation distance, for both the waves of $A = 0.5$ m and $A = 4$ m. Looking at figure A1 we conclude that there is not a convincing gain in accuracy by using a finer mesh, which can be explained by the generally long wave lengths of tsunami waves.

| | | | $s = 200m$ | | $s = 6400m$ | |
|---|---|---|---|---|---|---|
| ID | $A_T$ $[m^2]$ | $N_{\text{cells}}$ | $A = 0.5$ | $A = 4$ | $A = 0.5$ | $A = 4$ |
| R1 | 96 | 2856 | -2.77e-5 | -1.09e-3 | -6.52e-4 | -3.52e-2 |
| R2 | 48 | 8224 | -2.03e-5 | -1.06e-3 | -6.45e-4 | -3.52e-2 |
| R3 | 24 | 12.2k | -2.05e-5 | -1.07e-3 | -6.45e-4 | -3.52e-2 |
| R4 | 12 | 28k | -2.07e-5 | -1.09e-3 | -6.45e-4 | -3.52e-2 |
| R5 | 3 | 100k | -2.10e-5 | -1.04e-3 | -6.45e-4 | -3.52e-2 |
| R6 | 0.75 | 0.4M | -1.40e-5 | -9.39e-4 | -6.38e-4 | -3.51e-2 |
| R7 | 0.1875 | 1.6M | -1.46e-5 | -5.88e-4 | -6.39e-4 | -3.47e-2 |

**Table A2.** Percentage of the maximum water height error $A^{t,s}_{max}$ for several mesh refinements, both $A = 0.5m$ and $A = 4m$ and $h_{ref} =$ 100m.

465 ## Appendix B: Error tables for Mesh sensitivity

In this paragraph we show tables for the tests presented in appendix part A. Th tables report the water height error between Basement (BM) and GeoClaw (GC), and Basement and BoussClaw, respectively, at each gauge and for each mesh resolution.

https://doi.org/10.5194/egusphere-2026-2890
Preprint. Discussion started: 16 July 2026


| $h_{ref}[m]$, $s[m]$ | G | $\max_{t,Gauge\#}\left(h^{\mathrm{BM}} - h^{\mathrm{GC}}\right)$ $A$ $[m]$ 0.1 | 0.4 | 1.0 | 6.0 |
|---|---|---|---|---|---|
| 40, 800 | 1 | 0.0005 | 0.0061 | - | - |
| | 2 | - | - | - | - |
| | 3 | 0.0011 | 0.0029 | - | - |
| 80,800 | 1 | 0.0003 | 0.0061 | 0.0131 | 0.1343 |
| | 2 | 0.0006 | 0.0054 | 0.041 | 0.5141 |
| | 3 | 0.0007 | 0.0029 | -0.0258 | - |
| 120, 1600 | 1 | 0.0001 | 0.0040 | 0.0083 | 0.0759 |
| | 2 | -0.0001 | 0.002 | 0.0194 | 0.4477 |
| | 3 | 0.0001 | 0.002 | -0.0165 | 0.4822 |
| 160,3200 | 1 | 0 | 0.0009 | 0.0035 | 0.0498 |
| | 2 | 0.0004 | 0.0022 | 0.0121 | 0.4121 |
| | 3 | -0.0032 | 0.0015 | -0.0104 | 0.0176 |
| 200,6400 | 1 | 0.0004 | 0.0003 | 0.0024 | 0.0353 |
| | 2 | 0.0001 | 0.0013 | 0.0084 | 0.3955 |
| | 3 | 0.0003 | 0.0006 | -0.0055 | -0.2321 |

**Table B1.** Computations for combinations of still water reference $h_{ref}$ and propagation distances **S** for initial amplitudes $A = [0.1, 0.4, 1, 6]$ $m$. Table values report the water height error between Basement (BM) and GeoClaw (GC) at each gauge for different mesh resolutions.

https://doi.org/10.5194/egusphere-2026-2890
Preprint. Discussion started: 16 July 2026


| | | $\max_{t,Gauge\#}\left(h^{\mathrm{BM}}-h^{\mathrm{BC}}\right)$ | | | |
|---|---|---|---|---|---|
| | | $A$ $[m]$ | | | |
| $h_{ref}[m]$, $s[m]$ | G | 0.1 | 0.4 | 1.0 | 6.0 |
| 40, 800 | 1 | 0.0011 | 0.0061 | - | 0.3641 |
| | 2 | 0.0062 | 0.0054 | - | 0.8532 |
| | 3 | 0.0025 | 0.0029 | - | 0.7020 |
| 80,800 | 1 | 0.0003 | 0.0061 | 0.0132 | 0.1343 |
| | 2 | 0.0006 | 0.0054 | 0.0412 | 0.514 |
| | 3 | 0.0007 | 0.0029 | -0.0258 | - |
| 120, 1600 | 1 | 0.0001 | 0.0043 | 0.0083 | 0.0075 |
| | 2 | -0.0001 | 0.002 | 0.0194 | 0.9506 |
| | 3 | 0.0001 | 0.002 | -0.0165 | 0.4825 |
| 160,3200 | 1 | 0 | 0.0009 | 0.0035 | 0.0498 |
| | 2 | 0.0004 | 0.0022 | 0.0121 | 0.4121 |
| | 3 | -0.0032 | 0.0015 | -0.0104 | 0.0176 |
| 200,6400 | 1 | 0.0004 | 0.0004 | 0.0024 | 0.0128 |
| | 2 | 0.0001 | 0.233 | 0.0084 | 0.4121 |
| | 3 | 0.0003 | 0.279 | -0.0055 | -0.0608 |

**Table B2.** Computations for combinations of still water reference $h_{ref}$ and propagation distances **S** for initial amplitudes $A = [0.1, 0.4, 1, 6]$ $m$. Table values report the water height error between Basement (BM) and BoussClaw (BC) at each gauge for different mesh resolutions.

## Appendix C: Error tables for 1st order of accuracy calculations

Here we report the error tables for the tests presented in section 5.1.1. The tables show for each set of amplitude and still water reference depth the errors for the maximum amplitude ($A^{t,s}_{max} = \frac{max_t A_s}{max_t A_{ref}} \times 100 - 100$) and the wave period distortion ($\Delta t_s = \frac{\Delta t_{\mathrm{ref}}}{\Delta t_{ref}} \times 100 - 100$). The values with subscript "ref" indicate the values computed at gauge #1: located at $1.5L_w$ m with GeoClaw and BoussClaw, and at 0 m in BASEMENT (input wave is the height of the wave at gauge #1 obtained in GeoClaw).

https://doi.org/10.5194/egusphere-2026-2890
Preprint. Discussion started: 16 July 2026


| $A$ $[m]$ | $\varepsilon$ | | [%] | 50 | 100 | 200 | 400 | 800 | 1600 | 3200 | 6400 |
|---|---|---|---|---|---|---|---|---|---|---|---|
| | | | | s $[m]$ | | | | | | | |
| 0.1 | 0.004 | BM3 | $A^{t,s}_{max}$ | 0 | 0 | 0 | 0 | -0.001 | -0.002 | -0.003 | -0.007 |
| | | | $\Delta t_s$ | 0.292 | 0.292 | 0.365 | 0.292 | -0.073 | -16.447 | -16.813 | -17.471 |
| | | GC | $A^{t,s}_{max}$ | 0 | 0 | 0 | -0.001 | -0.001 | -0.002 | -0.005 | -0.009 |
| | | | $\Delta t_s$ | 0.283 | 0.576 | 0.712 | 0.858 | 1.089 | 1.456 | 1.822 | 2.189 |
| | | BC | $A^{t,s}_{max}$ | 0 | 0 | 0 | -0.001 | -0.001 | -0.002 | -0.005 | -0.009 |
| | | | $\Delta t_s$ | 0.314 | 0.679 | 1.043 | 1.699 | 2.428 | 3.303 | 4.459 | 6.074 |
| 0.5 | 0.02 | BM3 | $A^{t,s}_{max}$ | -0.001 | -0.002 | -0.004 | -0.009 | -0.017 | -0.034 | -0.066 | -0.128 |
| | | | $\Delta t_s$ | 0.997 | 1.329 | 1.495 | 1.661 | 1.495 | 0.332 | -2.326 | -8.472 |
| | | GC | $A^{t,s}_{max}$ | -0.002 | -0.003 | -0.007 | -0.014 | -0.027 | -0.053 | -0.102 | -0.191 |
| | | | $\Delta t_s$ | 0.998 | 1.471 | 1.829 | 2.327 | 2.826 | 2.992 | 2.161 | -0.164 |
| | | BC | $A^{t,s}_{max}$ | -0.002 | -0.003 | -0.007 | -0.014 | -0.027 | -0.052 | -0.096 | -0.172 |
| | | | $\Delta t_s$ | 2.822 | 4.614 | 6.57 | 9.014 | 12.11 | 16.021 | 20.909 | 26.776 |
| 1.0 | 0.04 | BM3 | $A^{t,s}_{max}$ | -0.005 | -0.009 | -0.018 | -0.035 | -0.07 | -0.139 | -0.276 | -0.585 |
| | | | $\Delta t_s$ | 1.675 | 1.675 | 2.153 | 1.914 | 0.718 | -2.632 | -10.048 | -21.77 |
| | | GC | $A^{t,s}_{max}$ | -0.006 | -0.013 | -0.025 | -0.05 | -0.098 | -0.191 | -0.371 | -0.72 |
| | | | $\Delta t_s$ | 1.438 | 1.916 | 2.634 | 2.873 | 2.634 | 0.72 | -3.108 | -10.524 |
| | | BC | $A^{t,s}_{max}$ | -0.006 | -0.013 | -0.025 | -0.049 | -0.094 | -0.175 | -0.313 | -0.531 |
| | | | $\Delta t_s$ | 4.687 | 7.915 | 11.374 | 15.524 | 20.367 | 26.592 | 33.703 | 42.042 |
| 2.0 | 0.08 | BM3 | $A^{t,s}_{max}$ | -0.015 | -0.03 | -0.064 | -0.126 | -0.252 | -0.55 | -1.382 | -2.611 |
| | | | $\Delta t_s$ | 1.736 | 1.736 | 1.389 | -0.347 | -5.208 | -14.236 | -27.778 | -47.917 |
| | | GC | $A^{t,s}_{max}$ | -0.022 | -0.044 | -0.088 | -0.175 | -0.351 | -0.734 | -1.568 | -2.745 |
| | | | $\Delta t_s$ | 2.094 | 2.791 | 2.791 | 1.746 | -1.39 | -7.376 | -17.419 | -31.764 |
| | | BC | $A^{t,s}_{max}$ | -0.022 | -0.044 | -0.086 | -0.165 | -0.307 | -0.547 | -0.93 | -1.507 |
| | | | $\Delta t_s$ | 7.611 | 12.828 | 18.64 | 25.22 | 32.394 | 41.141 | 50.598 | 61.742 |
| 4.0 | 0.16 | BM3 | $A^{t,s}_{max}$ | -0.053 | -0.103 | -0.209 | -0.458 | -1.205 | -3.116 | -5.382 | -7.367 |
| | | | $\Delta t_s$ | 1.554 | 0.518 | -2.073 | -7.772 | -18.135 | -35.233 | -62.694 | -72.021 |
| | | GC | $A^{t,s}_{max}$ | -0.073 | -0.147 | -0.3 | -0.647 | -1.565 | -3.417 | -5.595 | -7.531 |
| | | | $\Delta t_s$ | 2.188 | 2.188 | 1.043 | -3.412 | -11.194 | -23.848 | -45.016 | -55.909 |
| | | BC | $A^{t,s}_{max}$ | -0.072 | -0.141 | -0.27 | -0.499 | -0.892 | -1.521 | -2.493 | -3.937 |
| | | | $\Delta t_s$ | 11.614 | 19.654 | 28.791 | 38.023 | 48.272 | 59.163 | 70.335 | 84.183 |
| 8.0 | 0.32 | BM3 | $A^{t,s}_{max}$ | -0.131 | -0.3 | -0.965 | -2.856 | -6.256 | -9.912 | -13.223 | -15.858 |
| | | | $\Delta t_s$ | 0.794 | -2.381 | -10.317 | -20.635 | -42.857 | -78.571 | -75.397 | -66.667 |
| | | GC | $A^{t,s}_{max}$ | -0.257 | -0.562 | -1.37 | -3.384 | -6.641 | -10.246 | -13.461 | -16.018 |
| | | | $\Delta t_s$ | 2.389 | 0.81 | -3.377 | -12.676 | -29.356 | -60.313 | -59.675 | -45.882 |
| | | BC | $A^{t,s}_{max}$ | -0.209 | -0.397 | -0.734 | -1.307 | -2.222 | -3.653 | -5.897 | -9.209 |
| | | | $\Delta t_s$ | 15.919 | 28.467 | 41.315 | 54.337 | 66.702 | 78.428 | 90.797 | 109.681 |

**Table C1.** Computations for the still water reference $\mathbf{h_{ref} = 25m}$ and diverse amplitudes. Table values report for each propagation distance $s$ the relative amplitude error $A^{t,s}_{max}$ and phase shift $\Delta t_s$ for BASEMENT (BM3), GeoClaw (GC) and BoussClaw (BC).

https://doi.org/10.5194/egusphere-2026-2890
Preprint. Discussion started: 16 July 2026


| | | | | s $[m]$ | | | | | | | |
|---|---|---|---|---|---|---|---|---|---|---|---|
| $A$ $[m]$ | $\varepsilon$ | | [%] | 50 | 100 | 200 | 400 | 800 | 1600 | 3200 | 6400 |
| 0.1 | 0.002 | BM3 | $A^{t,s}_{max}$ | 0 | 0 | 0 | 0 | 0 | 0 | 0 | 0 |
| | | | $\Delta t_s$ | 0.109 | 0.146 | 0.182 | 0.182 | 0.146 | -23.568 | -23.605 | -23.714 |
| | | GC | $A^{t,s}_{max}$ | 0 | 0 | 0 | 0 | 0 | 0 | 0 | -0.001 |
| | | | $\Delta t_s$ | 0.147 | 0.095 | 0.227 | 0.3 | 0.41 | 0.556 | 0.739 | 0.936 |
| | | BC | $A^{t,s}_{max}$ | 0 | 0 | 0 | 0 | 0 | 0 | 0 | -0.001 |
| | | | $\Delta t_s$ | 0.064 | 0.334 | 0.517 | 0.772 | 1.1 | 1.502 | 2.122 | 2.888 |
| 0.5 | 0.01 | BM3 | $A^{t,s}_{max}$ | 0 | 0 | 0 | -0.001 | -0.001 | -0.003 | -0.005 | -0.01 |
| | | | $\Delta t_s$ | 0.411 | 0.493 | 0.74 | 0.822 | 1.069 | 1.069 | 0.822 | -0.329 |
| | | GC | $A^{t,s}_{max}$ | 0 | 0 | 0 | -0.001 | -0.002 | -0.004 | -0.007 | -0.015 |
| | | | $\Delta t_s$ | 0.363 | 0.577 | 0.742 | 0.988 | 1.4 | 1.68 | 1.927 | 1.894 |
| | | BC | $A^{t,s}_{max}$ | 0 | 0 | 0 | -0.001 | -0.002 | -0.004 | -0.007 | -0.015 |
| | | | $\Delta t_s$ | 1.023 | 2.05 | 3.272 | 4.657 | 6.319 | 8.404 | 10.93 | 14.14 |
| 1.0 | 0.02 | BM3 | $A^{t,s}_{max}$ | 0 | -0.001 | -0.001 | -0.003 | -0.005 | -0.01 | -0.02 | -0.04 |
| | | | $\Delta t_s$ | 0.469 | 0.822 | 0.939 | 1.174 | 1.291 | 0.939 | -0.352 | -3.404 |
| | | GC | $A^{t,s}_{max}$ | 0 | -0.001 | -0.002 | -0.004 | -0.007 | -0.014 | -0.028 | -0.055 |
| | | | $\Delta t_s$ | 0.588 | 0.823 | 1.081 | 1.433 | 1.716 | 1.833 | 1.363 | -0.469 |
| | | BC | $A^{t,s}_{max}$ | 0 | -0.001 | -0.002 | -0.004 | -0.007 | -0.014 | -0.028 | |
| | | | $\Delta t_s$ | 1.677 | 3.404 | 5.592 | 7.942 | 10.774 | 14.297 | 18.489 | |
| 2.0 | 0.04 | BM3 | $A^{t,s}_{max}$ | -0.001 | -0.002 | -0.004 | -0.009 | -0.017 | -0.033 | -0.066 | -0.135 |
| | | | $\Delta t_s$ | 0.676 | 1.014 | 1.014 | 1.014 | 0.507 | -1.351 | -5.743 | -15.034 |
| | | GC | $A^{t,s}_{max}$ | -0.002 | -0.003 | -0.007 | -0.013 | -0.026 | -0.052 | -0.103 | -0.21 |
| | | | $\Delta t_s$ | 0.778 | 1.116 | 1.454 | 1.623 | 1.454 | 0.371 | -2.873 | -9.706 |
| | | BC | $A^{t,s}_{max}$ | -0.002 | -0.003 | -0.007 | -0.013 | -0.026 | -0.051 | -0.095 | -0.173 |
| | | | $\Delta t_s$ | 2.699 | 5.402 | 9.149 | 13.126 | 17.687 | 23.159 | 29.579 | 36.94 |
| 4.0 | 0.08 | BM3 | $A^{t,s}_{max}$ | -0.004 | -0.008 | -0.017 | -0.035 | -0.071 | -0.143 | -0.345 | -1.235 |
| | | | $\Delta t_s$ | 0.988 | 1.235 | 1.235 | 0.247 | -2.222 | -8.148 | -19.506 | -34.815 |
| | | GC | $A^{t,s}_{max}$ | -0.006 | -0.011 | -0.022 | -0.045 | -0.089 | -0.182 | -0.434 | -1.318 |
| | | | $\Delta t_s$ | 0.99 | 1.237 | 1.237 | 0.743 | -1.089 | -6.027 | -15.553 | -28.537 |
| | | BC | $A^{t,s}_{max}$ | -0.006 | -0.012 | -0.024 | -0.047 | -0.09 | -0.169 | -0.303 | -0.526 |
| | | | $\Delta t_s$ | 4.186 | 8.335 | 14.328 | 20.648 | 27.831 | 35.764 | 44.62 | 53.743 |
| 8.0 | 0.16 | BM3 | $A^{t,s}_{max}$ | -0.015 | -0.026 | -0.052 | -0.114 | -0.239 | -1.063 | -3.118 | -5.453 |
| | | | $\Delta t_s$ | 0.738 | 0.738 | -0.738 | -4.428 | -12.177 | -23.985 | -42.804 | -73.063 |
| | | GC | $A^{t,s}_{max}$ | -0.017 | -0.034 | -0.068 | -0.139 | -0.319 | -1.196 | -3.239 | -5.548 |
| | | | $\Delta t_s$ | 0.949 | 0.742 | -0.158 | -3.111 | -9.959 | -20.292 | -36.528 | -63.254 |
| | | BC | $A^{t,s}_{max}$ | -0.02 | -0.04 | -0.079 | -0.15 | -0.277 | -0.493 | -0.843 | -1.409 |
| | | | $\Delta t_s$ | 6.051 | 11.724 | 21.158 | 31.1 | 41.184 | 51.919 | 62.187 | 71.296 |

**Table C2.** Computations for the still water reference $\mathbf{h_{ref} = 50m}$ and diverse amplitudes. Table values report for each propagation distance $s$ the relative amplitude error $A^{t,s}_{max}$ and phase shift $\Delta t_s$ for BASEMENT (BM3), GeoClaw (GC) and BoussClaw (BC).

https://doi.org/10.5194/egusphere-2026-2890
Preprint. Discussion started: 16 July 2026


| $A$ $[m]$ | $\varepsilon$ | | [%] | 50 | 100 | 200 | 400 | 800 | 1600 | 3200 | 6400 |
|---|---|---|---|---|---|---|---|---|---|---|---|
| | | | | s $[m]$ | | | | | | | |
| 0.1 | 0.001 | BM3 | $A^{t,s}_{max}$ | 0 | 0 | 0 | 0 | 0 | 0 | 0 | 0 |
| | | | $\Delta t_s$ | 0.036 | 0.055 | 0.055 | 0.036 | -4.483 | -4.446 | -4.446 | -4.574 |
| | | GC | $A^{t,s}_{max}$ | 0 | 0 | 0 | 0 | 0 | 0 | 0 | 0 |
| | | | $\Delta t_s$ | 0 | 0.008 | 0.008 | 0.016 | 0.022 | 0.055 | 0.115 | -0.326 |
| | | BC | $A^{t,s}_{max}$ | 0 | 0 | 0 | 0 | 0 | 0 | 0 | 0 |
| | | | $\Delta t_s$ | -0.403 | -0.67 | -1.135 | -1.577 | -2.016 | -2.401 | -2.785 | -3.115 |
| 0.5 | 0.005 | BM3 | $A^{t,s}_{max}$ | 0 | 0 | 0 | 0 | 0 | 0 | 0 | -0.001 |
| | | | $\Delta t_s$ | 0.123 | 0.205 | 0.286 | 0.368 | 0.491 | 0.655 | 0.736 | 0.696 |
| | | GC | $A^{t,s}_{max}$ | 0 | 0 | 0 | 0 | 0 | 0 | 0 | -0.001 |
| | | | $\Delta t_s$ | 0.1 | -0.14 | -0.122 | -0.041 | -0.099 | -0.081 | -0.058 | -0.286 |
| | | BC | $A^{t,s}_{max}$ | 0 | 0 | 0 | 0 | 0 | 0 | 0 | -0.001 |
| | | | $\Delta t_s$ | -0.442 | -0.523 | -0.302 | -0.075 | 0.03 | 0.292 | 0.798 | 1.049 |
| 1.0 | 0.01 | BM3 | $A^{t,s}_{max}$ | 0 | 0 | 0 | 0 | 0 | -0.001 | -0.001 | -0.003 |
| | | | $\Delta t_s$ | 0.233 | 0.349 | 0.407 | 0.582 | 0.698 | 0.814 | 0.756 | 0.407 |
| | | GC | $A^{t,s}_{max}$ | 0 | 0 | 0 | 0 | 0 | -0.001 | -0.002 | -0.004 |
| | | | $\Delta t_s$ | 0.151 | 0.068 | 0.175 | 0.267 | 0.184 | 0.267 | 0.151 | -0.257 |
| | | BC | $A^{t,s}_{max}$ | 0 | 0 | 0 | 0 | 0 | -0.001 | -0.002 | -0.004 |
| | | | $\Delta t_s$ | -0.27 | 0.051 | 0.71 | 1.295 | 1.814 | 2.727 | 3.683 | 5.067 |
| 2.0 | 0.02 | BM3 | $A^{t,s}_{max}$ | 0 | 0 | 0 | -0.001 | -0.001 | -0.002 | -0.005 | -0.01 |
| | | | $\Delta t_s$ | 0.332 | 0.415 | 0.498 | 0.664 | 0.747 | 0.747 | 0.249 | -1.245 |
| | | GC | $A^{t,s}_{max}$ | 0 | 0 | 0 | -0.001 | -0.002 | -0.004 | -0.007 | -0.014 |
| | | | $\Delta t_s$ | 0.049 | 0.132 | 0.215 | 0.333 | 0.298 | 0.062 | -0.532 | -2.11 |
| | | BC | $A^{t,s}_{max}$ | 0 | 0 | 0 | -0.001 | -0.002 | -0.004 | -0.008 | -0.014 |
| | | | $\Delta t_s$ | 0.06 | 0.841 | 2.05 | 3.156 | 4.623 | 6.321 | 8.371 | 10.816 |
| 4.0 | 0.04 | BM3 | $A^{t,s}_{max}$ | 0 | -0.001 | -0.001 | -0.002 | -0.005 | -0.009 | -0.018 | -0.036 |
| | | | $\Delta t_s$ | 0.478 | 0.598 | 0.718 | 0.718 | 0.598 | -0.239 | -2.392 | -7.416 |
| | | GC | $A^{t,s}_{max}$ | 0 | -0.001 | -0.002 | -0.003 | -0.006 | -0.013 | -0.026 | -0.051 |
| | | | $\Delta t_s$ | 0.29 | 0.26 | 0.31 | 0.24 | -0.049 | -0.935 | -3.207 | -8.079 |
| | | BC | $A^{t,s}_{max}$ | 0 | -0.001 | -0.002 | -0.004 | -0.007 | -0.014 | -0.027 | -0.05 |
| | | | $\Delta t_s$ | 0.353 | 1.487 | 3.319 | 5.327 | 7.605 | 10.301 | 13.518 | 17.33 |
| 8.0 | 0.08 | BM3 | $A^{t,s}_{max}$ | -0.001 | -0.002 | -0.005 | -0.009 | -0.018 | -0.036 | -0.072 | -0.19 |
| | | | $\Delta t_s$ | 0.524 | 0.699 | 0.699 | 0.524 | -0.874 | -4.021 | -10.839 | -24.126 |
| | | GC | $A^{t,s}_{max}$ | -0.001 | -0.003 | -0.006 | -0.011 | -0.022 | -0.044 | -0.09 | -0.238 |
| | | | $\Delta t_s$ | 0.351 | 0.383 | 0.248 | -0.173 | -1.572 | -4.822 | -11.712 | -24.577 |
| | | BC | $A^{t,s}_{max}$ | -0.002 | -0.004 | -0.007 | -0.014 | -0.027 | -0.052 | -0.096 | -0.17 |
| | | | $\Delta t_s$ | 1.328 | 3.311 | 6.605 | 10.704 | 15.129 | 20.176 | 25.845 | 31.964 |

**Table C3.** Computations for the still water reference $\mathbf{h_{ref} = 100m}$ and diverse amplitudes. Table values report for each propagation distance $s$ the relative amplitude error $A^{t,s}_{max}$ and phase shift $\Delta t_s$ for BASEMENT (BM3), GeoClaw (GC) and BoussClaw (BC).

https://doi.org/10.5194/egusphere-2026-2890
Preprint. Discussion started: 16 July 2026


| $A$ $[m]$ | $\varepsilon$ | | [%] | s $[m]$ | | | | | | | |
|---|---|---|---|---|---|---|---|---|---|---|---|
| | | | | 50 | 100 | 200 | 400 | 800 | 1600 | 3200 | 6400 |
| 0.5 | 0.0025 | BM3 | $A^{t,s}_{max}$ | 0 | 0 | 0 | 0 | 0 | 0 | 0 | 0 |
| | | | $\Delta t_s$ | 0.082 | 0.102 | 0.122 | 0.184 | 0.224 | 0.286 | 0.347 | 0.408 |
| | | GC | $A^{t,s}_{max}$ | 0 | 0 | 0 | 0 | 0 | 0 | 0 | 0 |
| | | | $\Delta t_s$ | 0.016 | 0.029 | 0.041 | 0.07 | -0.155 | -0.12 | -0.061 | 0.149 |
| | | BC | $A^{t,s}_{max}$ | 0 | 0 | 0 | 0 | 0 | 0 | 0 | 0 |
| | | | $\Delta t_s$ | -0.221 | -0.397 | -0.254 | -0.105 | 0.018 | 0.181 | 0.432 | 0.419 |
| 1.0 | 0.005 | BM3 | $A^{t,s}_{max}$ | 0 | 0 | 0 | 0 | 0 | 0 | 0 | 0 |
| | | | $\Delta t_s$ | 0.087 | 0.116 | 0.145 | 0.231 | 0.318 | 0.376 | 0.463 | 0.492 |
| | | GC | $A^{t,s}_{max}$ | 0 | 0 | 0 | 0 | 0 | 0 | 0 | 0 |
| | | | $\Delta t_s$ | 0.047 | 0.067 | 0.087 | 0.145 | 0.076 | 0.174 | 0.212 | 0.249 |
| | | BC | $A^{t,s}_{max}$ | 0 | 0 | 0 | 0 | 0 | 0 | 0 | 0 |
| | | | $\Delta t_s$ | -0.255 | -0.215 | 0.082 | 0.495 | 0.89 | 1.302 | 1.899 | 2.476 |
| 2.0 | 0.01 | BM3 | $A^{t,s}_{max}$ | 0 | 0 | 0 | 0 | 0 | 0 | 0 | -0.001 |
| | | | $\Delta t_s$ | 0.123 | 0.164 | 0.247 | 0.329 | 0.452 | 0.535 | 0.576 | 0.493 |
| | | GC | $A^{t,s}_{max}$ | 0 | 0 | 0 | 0 | 0 | 0 | 0 | -0.001 |
| | | | $\Delta t_s$ | 0.087 | 0.124 | 0.21 | 0.182 | 0.223 | 0.276 | 0.198 | 0.116 |
| | | BC | $A^{t,s}_{max}$ | 0 | 0 | 0 | 0 | 0 | 0 | 0 | -0.001 |
| | | | $\Delta t_s$ | -0.307 | 0.047 | 0.63 | 1.368 | 2.208 | 3.162 | 4.385 | 5.742 |
| 4.0 | 0.02 | BM3 | $A^{t,s}_{max}$ | 0 | 0 | 0 | 0 | 0 | -0.001 | -0.001 | -0.003 |
| | | | $\Delta t_s$ | 0.176 | 0.235 | 0.352 | 0.47 | 0.587 | 0.528 | 0.352 | -0.235 |
| | | GC | $A^{t,s}_{max}$ | 0 | 0 | 0 | 0 | 0 | -0.001 | -0.002 | -0.003 |
| | | | $\Delta t_s$ | 0.159 | 0.159 | 0.201 | 0.259 | 0.294 | 0.183 | -0.093 | -0.746 |
| | | BC | $A^{t,s}_{max}$ | 0 | 0 | 0 | 0 | 0 | -0.001 | -0.002 | -0.003 |
| | | | $\Delta t_s$ | -0.117 | 0.401 | 1.317 | 2.664 | 4.294 | 6.097 | 8.342 | 10.761 |
| 8.0 | 0.04 | BM3 | $A^{t,s}_{max}$ | | 0 0 | 0 | -0.001 | -0.001 | -0.002 | -0.005 | -0.01 |
| | | | $\Delta t_s$ | 0.338 | 0.423 | 0.508 | 0.508 | 0.508 | 0.085 | -0.846 | -3.299 |
| | | GC | $A^{t,s}_{max}$ | 0 | 0 | 0 | -0.001 | -0.002 | -0.003 | -0.006 | -0.012 |
| | | | $\Delta t_s$ | 0.17 | 0.195 | 0.264 | 0.23 | 0.095 | -0.337 | -1.377 | -3.89 |
| | | BC | $A^{t,s}_{max}$ | 0 | 0 | 0 | -0.001 | -0.002 | -0.004 | -0.009 | -0.013 |
| | | | $\Delta t_s$ | 0.2 | 0.933 | 2.327 | 4.679 | 7.587 | 10.764 | 14.429 | 18.558 |

**Table C4.** Computations for the still water reference $\mathbf{h_{ref}} = \mathbf{200m}$ and diverse amplitudes. Table values report for each propagation distance $s$ the relative amplitude error $A^{t,s}_{max}$ and phase shift $\Delta t_s$ for BASEMENT (BM3), GeoClaw (GC) and BoussClaw (BC).

https://doi.org/10.5194/egusphere-2026-2890
Preprint. Discussion started: 16 July 2026


## Appendix D: Error tables for 2nd order of accuracy calculations

In this paragraph we report the error tables for the tests presented in section 5.1.2. The tables show for each set of amplitude and still water reference depth the errors for the maximum amplitude ($A^{t,s}_{max} = \frac{max_t A_s}{max_t A_{ref}} \times 100 - 100$) and the wave period distortion ($\Delta t_s = \frac{\Delta t_{\text{ref}}}{\Delta t_{ref}} \times 100 - 100$). The values with subscript "ref" indicate the values computed at gauge #1: located at $1.5L_w$ m with GeoClaw and BoussClaw, and at $0$ m in BASEMENT input wave is the height of the wave at gauge #1 obtained in GeoClaw).

https://doi.org/10.5194/egusphere-2026-2890
Preprint. Discussion started: 16 July 2026


| | | | | s $[m]$ | | | | | | | |
|---|---|---|---|---|---|---|---|---|---|---|---|
| $A\ [m]$ | $\varepsilon$ | | [%] | 50 | 100 | 200 | 400 | 800 | 1600 | 3200 | 6400 |
| 0.5 | 0.0025 | BM3 | $A^{t,s}_{max}$ | -0.001 | -0.002 | -0.004 | -0.009 | -0.017 | -0.034 | -0.066 | -0.128 |
| | | | $\Delta t_s$ | 0.997 | 1.329 | 1.495 | 1.661 | 1.495 | 0.332 | -2.326 | -8.472 |
| | | GC | $A^{t,s}_{max}$ | 0 | 0 | 0 | 0 | -0.001 | -0.001 | -0.002 | -0.004 |
| | | | $\Delta t_s$ | 0.668 | 0.335 | 0.335 | 0.002 | -1.332 | -3.332 | -8.165 | -17.499 |
| | | BC | $A^{t,s}_{max}$ | 0 | 0 | 0 | 0 | 0 | -0.001 | -0.001 | -0.002 |
| | | | $\Delta t_s$ | 2.796 | 4.589 | 6.407 | 8.851 | 11.621 | 14.88 | 18.791 | 23.354 |
| 1.0 | 0.005 | BM3 | $A^{t,s}_{max}$ | -0.005 | -0.009 | -0.018 | -0.035 | -0.07 | -0.139 | -0.276 | -0.585 |
| | | | $\Delta t_s$ | 1.675 | 1.675 | 2.153 | 1.914 | 0.718 | -2.632 | -10.048 | -21.77 |
| | | GC | $A^{t,s}_{max}$ | 0 | 0 | -0.001 | -0.002 | -0.003 | -0.006 | -0.01 | -0.255 |
| | | | $\Delta t_s$ | 0.482 | 0.242 | -0.477 | -1.676 | -4.833 | -11.469 | -24.659 | -41.725 |
| | | BC | $A^{t,s}_{max}$ | 0 | -0.001 | -0.001 | -0.002 | -0.003 | -0.005 | -0.009 | -0.013 |
| | | | $\Delta t_s$ | 4.687 | 7.915 | 11.143 | 15.063 | 19.675 | 24.978 | 30.743 | 36.315 |
| 2.0 | 0.01 | BM3 | $A^{t,s}_{max}$ | -0.015 | -0.03 | -0.064 | -0.126 | -0.252 | -0.55 | -1.382 | -2.611 |
| | | | $\Delta t_s$ | 1.736 | 1.736 | 1.389 | -0.347 | -5.208 | -14.236 | -27.778 | -47.917 |
| | | GC | $A^{t,s}_{max}$ | -0.001 | -0.002 | -0.004 | -0.007 | -0.013 | -0.084 | -1.113 | -2.479 |
| | | | $\Delta t_s$ | 0.705 | -0.348 | -2.102 | -6.313 | -15.085 | -30.236 | -49.121 | -78.947 |
| | | BC | $A^{t,s}_{max}$ | -0.002 | -0.003 | -0.007 | -0.013 | -0.021 | -0.033 | -0.047 | -0.057 |
| | | | $\Delta t_s$ | 7.548 | 12.762 | 18.303 | 24.169 | 31.013 | 38.183 | 45.027 | 49.915 |
| 4.0 | 0.02 | BM3 | $A^{t,s}_{max}$ | -0.053 | -0.103 | -0.209 | -0.458 | -1.205 | -3.116 | -5.382 | -7.367 |
| | | | $\Delta t_s$ | 1.554 | 0.518 | -2.073 | -7.772 | -18.135 | -35.233 | -62.694 | -72.021 |
| | | GC | $A^{t,s}_{max}$ | -0.004 | -0.007 | -0.015 | -0.039 | -0.979 | -3.125 | -5.491 | -7.565 |
| | | | $\Delta t_s$ | -0.519 | -3.14 | -8.796 | -19.279 | -33.955 | -57.543 | -94.137 | -92.662 |
| | | BC | $A^{t,s}_{max}$ | -0.01 | -0.019 | -0.033 | -0.059 | -0.089 | -0.114 | -0.117 | -0.091 |
| | | | $\Delta t_s$ | 11.101 | 19.469 | 27.739 | 36.833 | 45.564 | 53.011 | 58.066 | 59.904 |
| 8.0 | 0.04 | BM3 | $A^{t,s}_{max}$ | -0.131 | -0.3 - | 0.965 | -2.856 | -6.256 | -9.912 | -13.223 | -15.858 |
| | | | $\Delta t_s$ | 0.794 | -2.381 | -10.317 | -20.635 | -42.857 | -78.571 | -75.397 | -66.667 |
| | | GC | $A^{t,s}_{max}$ | -0.038 | -0.088 | -0.849 | -3.199 | -6.736 | -10.533 | -13.897 | -16.563 |
| | | | $\Delta t_s$ | -3.824 | -8.935 | -18.687 | -35.977 | -66.662 | -92.682 | -91.217 | -89.43 |
| | | BC | $A^{t,s}_{max}$ | -0.05 | -0.096 | -0.161 | -0.25 | -0.33 | -0.384 | -0.418 | -0.467 |
| | | | $\Delta t_s$ | 15.919 | 28.758 | 41.132 | 52.386 | 62.153 | 68.014 | 69.968 | 69.968 |

**Table D1.** Computations for the still water reference $\mathbf{h_{ref} = 25m}$ and diverse amplitudes. Table values report for each propagation distance $s$ the relative amplitude error $A^{t,s}_{max}$ and phase shift $\Delta t_s$ for BASEMENT (BM3), GeoClaw (GC) and BoussClaw (BC).

https://doi.org/10.5194/egusphere-2026-2890
Preprint. Discussion started: 16 July 2026


| | | | | s $[m]$ | | | | | | | |
|---|---|---|---|---|---|---|---|---|---|---|---|
| $A$ $[m]$ | $\varepsilon$ | | $[\%]$ | 50 | 100 | 200 | 400 | 800 | 1600 | 3200 | 6400 |
| 1.0 | 0.005 | BM3 | $A^{t,s}_{max}$ | 0 | -0.001 | -0.001 | -0.003 | -0.005 | -0.01 | -0.02 | -0.04 |
| | | | $\Delta t_s$ | 0.469 | 0.822 | 0.939 | 1.174 | 1.291 | 0.939 | -0.352 | -3.404 |
| | | GC | $A^{t,s}_{max}$ | 0 | 0 | 0 | 0 | 0 | 0 | -0.001 | -0.001 |
| | | | $\Delta t_s$ | 0.189 | 0.306 | 0.189 | 0.024 | -0.587 | -1.693 | -3.927 | -8.701 |
| | | BC | $A^{t,s}_{max}$ | 0 | 0 | 0 | 0 | 0 | 0 | -0.001 | -0.001 |
| | | | $\Delta t_s$ | 1.747 | 3.475 | 5.618 | 7.969 | 10.735 | 14.076 | 18.063 | 22.765 |
| 2.0 | 0.01 | BM3 | $A^{t,s}_{max}$ | -0.001 | -0.002 | -0.004 | -0.009 | -0.017 | -0.033 | -0.066 | -0.135 |
| | | | $\Delta t_s$ | 0.676 | 1.014 | 1.014 | 1.014 | 0.507 | -1.351 | -5.743 | -15.034 |
| | | GC | $A^{t,s}_{max}$ | 0 | 0 | 0 | 0 | -0.001 | -0.001 | -0.002 | -0.004 |
| | | | $\Delta t_s$ | 0.341 | 0.241 | 0.002 | -0.676 | -2.202 | -5.522 | -11.932 | -25.322 |
| | | BC | $A^{t,s}_{max}$ | 0 | 0 | 0 | -0.001 | -0.002 | -0.003 | -0.006 | -0.009 |
| | | | $\Delta t_s$ | 2.699 | 5.498 | 9.149 | 13.059 | 17.553 | 22.767 | 28.765 | 35.444 |
| 4.0 | 0.02 | BM3 | $A^{t,s}_{max}$ | -0.004 | -0.008 | -0.017 | -0.035 | -0.071 | -0.143 | -0.345 | -1.235 |
| | | | $\Delta t_s$ | 0.988 | 1.235 | 1.235 | 0.247 | -2.222 | -8.148 | -19.506 | -34.815 |
| | | GC | $A^{t,s}_{max}$ | 0 | 0 | -0.001 | -0.001 | -0.003 | -0.005 | -0.053 | -1.07 |
| | | | $\Delta t_s$ | 0.107 | -0.141 | -1.132 | -3.258 | -7.575 | -16.639 | -32.106 | -51.041 |
| | | BC | $A^{t,s}_{max}$ | -0.001 | -0.002 | -0.004 | -0.007 | -0.013 | -0.022 | -0.033 | -0.047 |
| | | | $\Delta t_s$ | 4.047 | 8.19 | 14.042 | 20.391 | 27.393 | 35.026 | 43.083 | 50.873 |
| 8.0 | 0.04 | BM3 | $A^{t,s}_{max}$ | -0.015 | -0.026 | -0.052 | -0.114 | -0.239 | -1.063 | -3.118 | -5.453 |
| | | | $\Delta t_s$ | 0.738 | 0.738 | -0.738 | -4.428 | -12.177 | -23.985 | -42.804 | -73.063 |
| | | GC | $A^{t,s}_{max}$ | -0.001 | -0.001 | -0.002 | -0.005 | -0.017 | -0.896 | -3.06 | -5.459 |
| | | | $\Delta t_s$ | -0.16 | -1.483 | -4.086 | -9.87 | -21.395 | -36.057 | -60.222 | -96.282 |
| | | BC | $A^{t,s}_{max}$ | -0.006 | -0.011 | -0.022 | | -0.037 | -0.067 | -0.103 -0.139 | -0.162 |
| | | | $\Delta t_s$ | 6.051 | 11.907 | 21.341 | 30.918 | 41.003 | 50.762 | 59.727 | 65.765 |

**Table D2.** Computations for the still water reference $\mathbf{h_{ref} = 50m}$ and diverse amplitudes. Table values report for each propagation distance $s$ the relative amplitude error $A^{t,s}_{max}$ and phase shift $\Delta t_s$ for BASEMENT (BM3), GeoClaw (GC) and BoussClaw (BC).

https://doi.org/10.5194/egusphere-2026-2890
Preprint. Discussion started: 16 July 2026


| $A$ $[m]$ | $\varepsilon$ | | $[\%]$ | s $[m]$ 50 | 100 | 200 | 400 | 800 | 1600 | 3200 | 6400 |
|---|---|---|---|---|---|---|---|---|---|---|---|
| 2.0 | 0.01 | BM3 | $A^{t,s}_{max}$ | 0 | 0 | 0 | -0.001 | -0.001 | -0.002 | -0.005 | -0.01 |
| | | | $\Delta t_s$ | 0.332 | 0.415 | 0.498 | 0.664 | 0.747 | 0.747 | 0.249 | -1.245 |
| | | GC | $A^{t,s}_{max}$ | 0 | 0 | 0 | 0 | 0 | 0 | 0 | 0 |
| | | | $\Delta t_s$ | 0.071 | 0.049 | 0.001 | -0.082 | -0.367 | -1.046 | -2.197 | -4.623 |
| | | BC | $A^{t,s}_{max}$ | 0 | 0 | 0 | 0 | 0 | 0 | -0.001 | 0 |
| | | | $\Delta t_s$ | 0.06 | 0.793 | 1.934 | 3.156 | 4.473 | 6.124 | 8.243 | 10.619 |
| 4.0 | 0.02 | BM3 | $A^{t,s}_{max}$ | 0 | -0.001 | -0.001 | -0.002 | -0.005 | -0.009 | -0.018 | -0.036 |
| | | | $\Delta t_s$ | 0.478 | 0.598 | 0.718 | 0.718 | 0.598 | -0.239 | -2.392 | -7.416 |
| | | GC | $A^{t,s}_{max}$ | 0 | 0 | 0 | 0 | 0 | 0 | 0 | -0.001 |
| | | | $\Delta t_s$ | 0.071 | 0.001 | -0.119 | -0.478 | -1.318 | -2.946 | -6.304 | -12.999 |
| | | BC | $A^{t,s}_{max}$ | 0 | 0 | 0 | 0 | -0.001 | -0.002 | -0.003 | -0.006 |
| | | | $\Delta t_s$ | 0.353 | 1.533 | 3.365 | 5.28 | 7.577 | 10.143 | 13.36 | 17.042 |
| 8.0 | 0.04 | BM3 | $A^{t,s}_{max}$ | -0.001 | -0.002 | -0.005 | -0.009 | -0.018 | -0.036 | -0.072 | -0.19 |
| | | | $\Delta t_s$ | 0.524 | 0.699 | 0.699 | 0.524 | -0.874 | -4.021 | -10.839 | -24.126 |
| | | GC | $A^{t,s}_{max}$ | 0 | 0 | 0 | 0 | 0 | -0.001 | -0.002 | -0.041 |
| | | | $\Delta t_s$ | 0.002 | -0.142 | -0.7 | -1.792 | -3.927 | -8.557 | -17.777 | -34.081 |
| | | BC | $A^{t,s}_{max}$ | 0 | -0.001 | -0.002 | -0.004 | -0.007 | -0.013 | -0.022 | -0.033 |
| | | | $\Delta t_s$ | 1.328 | 3.311 | 6.605 | 10.771 | 15.1 | 20.08 | 25.519 | 31.38 |

**Table D3.** Computations for the still water reference $\mathbf{h_{ref}} = \mathbf{100m}$ and diverse amplitudes. Table values report for each propagation distance $s$ the relative amplitude error $A^{t,s}_{max}$ and phase shift $\Delta t_s$ for BASEMENT (BM3), GeoClaw (GC) and BoussClaw (BC).

https://doi.org/10.5194/egusphere-2026-2890
Preprint. Discussion started: 16 July 2026


| $A$ $[m]$ | $\varepsilon$ | | [%] | s $[m]$ 50 | 100 | 200 | 400 | 800 | 1600 | 3200 | 6400 |
|---|---|---|---|---|---|---|---|---|---|---|---|
| 4.0 | 0.02 | BM3 | $A^{t,s}_{max}$ | 0 | 0 | 0 | 0 | 0 | -0.001 | -0.001 | -0.003 |
| | | | $\Delta t_s$ | 0.176 | 0.235 | 0.352 | 0.47 | 0.587 | 0.528 | 0.352 | -0.235 |
| | | GC | $A^{t,s}_{max}$ | 0 | 0 | 0 | 0 | 0 | 0 | 0 | 0 |
| | | | $\Delta t_s$ | 0.042 | 0.042 | 0.024 | -0.017 | -0.152 | -0.429 | -0.999 | -2.228 |
| | | BC | $A^{t,s}_{max}$ | 0 | 0 | 0 | 0 | 0 | 0 | 0 | 0 |
| | | | $\Delta t_s$ | -0.175 | 0.384 | 1.282 | 2.647 | 4.253 | 6.102 | 8.192 | 10.685 |
| 8.0 | 0.04 | BM3 | $A^{t,s}_{max}$ | 0 | 0 | 0 | -0.001 | -0.001 | -0.002 | -0.005 | -0.01 |
| | | | $\Delta t_s$ | 0.338 | 0.423 | 0.508 | 0.508 | 0.508 | 0.085 | -0.846 | -3.299 |
| | | GC | $A^{t,s}_{max}$ | 0 | 0 | 0 | 0 | 0 | 0 | 0 | 0 |
| | | | $\Delta t_s$ | 0.076 | 0.051 | -0.034 | -0.203 | -0.627 | -1.424 | -3.083 | -6.421 |
| | | BC | $A^{t,s}_{max}$ | 0 | 0 | 0 | 0 | 0 | -0.001 | -0.003 | -0.001 |
| | | | $\Delta t_s$ | 0.128 | 0.908 | 2.326 | 4.653 | 7.56 | 10.701 | 14.35 | 18.411 |

**Table D4.** Computations for the still water reference $\mathbf{h_{ref} = 200m}$ and diverse amplitudes. Table values report for each propagation distance $s$ the relative amplitude error $A^{t,s}_{max}$ and phase shift $\Delta t_s$ for BASEMENT (BM3), GeoClaw (GC) and BoussClaw (BC).

*Author contributions.* P.B. and D.V. designed the study, P.B. performed the numerical simulations, J.C.S. took over the project and wrote the
480 paper draft, D.V. edited the paper draft.

*Competing interests.* The authors declare that they have no conflict of interest.

*Acknowledgements.* P.B. was founded by the Swiss National Science Foundation under the Sinergia Project "Lake Tsunamis: Causes, Controls, and Hazard", project #171017, J.C.S. and D.V. by VAW, ETH Zurich. P.B. would like to give a special thanks to Dr. Jihwan Kim for the discussions on the BoussClaw solver.

https://doi.org/10.5194/egusphere-2026-2890
Preprint. Discussion started: 16 July 2026


## References

Ambrosi, D.: Approximation of shallow water equations by Roe's Riemann solver, International journal for numerical methods in fluids, 20, 157–168, 1995.

Bacigaluppi, P., Ricchiuto, M., and Bonneton, P.: Implementation and evaluation of breaking detection criteria for a hybrid Boussinesq model, Water Waves, pp. 1–35, https://doi.org/10.1007/s42286-019-00023-8, 2019.

Beakawi Al-Hashemi, H. M. and Baghabra Al-Amoudi, O. S.: A review on the angle of repose of granular materials, Powder Technology, 330, 397–417, https://doi.org/https://doi.org/10.1016/j.powtec.2018.02.003, 2018.

Berger, M. J., George, D. L., LeVeque, R. J., and Mandli, K. T.: The GeoClaw software for depth-averaged flows with adaptive refinement, Advances in Water Resources, 34, 1195–1206, https://doi.org/10.1016/j.advwatres.2011.02.016, 2011.

Boussinesq, J.: Théorie des ondes et des remous qui se propagent le long d'un canal rectangulaire horizontal, en communiquant au liquide contenu dans ce canal des vitesses sensiblement pareilles de la surface au fond., Journal de mathématiques pures et appliquées, pp. 55–108, 1872.

Brocchini, M.: A reasoned overview on Boussinesq-type models: the interplay between physics, mathematics and numerics, Proceedings of the Royal Society A: Mathematical, Physical and Engineering Sciences, 469, 20130 496, https://doi.org/10.1098/rspa.2013.0496, 2013.

Brocchini, M. and Dodd, N.: Nonlinear shallow water equation modeling for coastal engineering, Journal of waterway, port, coastal, and ocean engineering, 134, 104–120, https://doi.org/10.1061/(ASCE)0733-950X(2008)134:2(104), 2008.

Chan, I.-C. and Liu, P. L.-F.: On the runup of long waves on a plane beach, Journal of Geophysical Research: Oceans, 117, 2012.

Couston, L.-A., Mei, C. C., and Alam, M.-R.: Landslide tsunamis in lakes, Journal of Fluid Mechanics, 772, 784–804, 2015.

Didenkulova, I. and Pelinovsky, E.: Runup of tsunami waves in U-shaped bays, Pure and applied geophysics, 168, 1239–1249, 2011.

Fathianpour, A., Wilkinson, S., Babaeian Jelodar, M., and Evans, B.: Reducing the vulnerability of tourists to tsunami: challenges for decision-makers, Natural Hazards, 118, 1315–1339, 2023.

Fuchs, H.: Solitary impulse wave run-up and overland flow, Ph.D. thesis, ETH Zurich, 2013.

Gariano, S. L. and Guzzetti, F.: Landslides in a changing climate, Earth-science reviews, 162, 227–252, 2016.

George, D. L.: Augmented Riemann solvers for the shallow water equations over variable topography with steady states and inundation, Journal of Computational Physics, 227, 3089–3113, https://doi.org/10.1016/j.jcp.2007.10.027, 2008.

Goring, D. G. and Raichlen, F.: Tsunamis–the propagation of long waves onto a shelf, 1978.

Hall, J. V., Watts, G. M., et al.: Laboratory investigation of the vertical rise of solitary waves on impermeable slopes, https://archive.org/stream/shoreprotectionm02unit/shoreprotectionm02unit_djvu.txt, 1953.

Hammack, J. L.: A note on tsunamis: their generation and propagation in an ocean of uniform depth, Journal of Fluid Mechanics, 60, 769–799, 1973.

Hammack Jr, J. L. and Raichlen, F.: Tsunami generation and propagation, in: Coastal Engineering 1972, pp. 2589–2608, 1972.

Harbitz, C.: Model simulations of tsunamis generated by the Storegga slides, Marine geology, 105, 1–21, https://doi.org/10.1016/0025-3227(92)90178-K, 1992.

Harbitz, C., Glimsdal, S., Løvholt, F., Kveldsvik, V., Pedersen, G., and Jensen, A.: Rockslide tsunamis in complex fjords: From an unstable rock slope at Åkerneset to tsunami risk in western Norway, Coastal engineering, 88, 101–122, 2014.

Heinrich, P., Piatanesi, A., and Hébert, H.: Numerical modelling of tsunami generation and propagation from submarine slumps: the 1998 Papua New Guinea event, Geophysical Journal International, 145, 97–111, 2001.

Hilbe, M. and Anselmetti, F. S.: Mass movement-induced tsunami hazard on perialpine Lake Lucerne (Switzerland): scenarios and numerical experiments, Pure and Applied Geophysics, 172, 545–568, https://doi.org/10.1007/s00024-014-0907-7, 2015.

Hock, R., Rasul, G., Adler, C., Cáceres, B., Gruber, S., Hirabayashi, Y., Jackson, M., Kääb, A., Kang, S., Kutuzov, S., et al.: High mountain areas, in: IPCC special report on the ocean and cryosphere in a changing climate, pp. 131–202, H.-O. Pörtner, DC Roberts, V. Masson-Delmotte, P. Zhai, M. Tignor, E . . . , 2019.

Hoffmann, G. and Reicherter, K.: Geohazards: Coastal Disasters, pp. 276–283, Springer Netherlands, Dordrecht, https://doi.org/10.1007/978-94-007-6238-1_169, 2016.

Jacquemart, M., Weber, S., Chiarle, M., Chmiel, M., Cicoira, A., Corona, C., Eckert, N., Gaume, J., Giacona, F., Hirschberg, J., et al.: Detecting the impact of climate change on alpine mass movements in observational records from the European Alps, Earth-Science Reviews, 258, 104 886, 2024.

Jiang, L. and LeBlond, P. H.: The coupling of a submarine slide and the surface waves which it generates, Journal of Geophysical Research: Oceans, 97, 12 731–12 744, https://doi.org/10.1029/92JC00912, 1992.

Kazolea, M. and Ricchiuto, M.: On wave breaking for Boussinesq-type models, Ocean Modelling, 123, 16 – 39, https://doi.org/https://doi.org/10.1016/j.ocemod.2018.01.003, 2018.

Kim, J., Pedersen, G. K., Løvholt, F., and LeVeque, R. J.: A Boussinesq type extension of the GeoClaw model-a study of wave breaking phenomena applying dispersive long wave models, Coastal engineering, 122, 75–86, https://doi.org/10.1016/j.coastaleng.2017.01.005, 2017.

Kim, J. W., Bai, K. J., Ertekin, R. C., and Webster, W. C.: A derivation of the Green-Naghdi equations for irrotational flows, Journal of Engineering Mathematics, 40, 17–42, 2001.

Kremer, K., Hilbe, M., Simpson, G., Decrouy, L., Wildi, W., and Girardclos, S.: Reconstructing 4000 years of mass movement and tsunami history in a deep peri-Alpine lake (Lake Geneva, France-Switzerland), Sedimentology, 62, 1305–1327, 2015.

Lannes, D. and Bonneton, P.: Derivation of asymptotic two-dimensional time-dependent equations for surface water wave propagation, Physics of fluids, 21, 016 601, https://doi.org/10.1063/1.3053183, 2009.

Lee, E. M. and Jones, D. K.: Qualitative and semi-quantitative risk assessment, in: Landslide Risk Assessment, pp. 97–128, ICE Publishing, https://doi.org/10.1680/lra.58019.097, 2014.

LeVeque, R. J., George, D. L., and Berger, M. J.: Tsunami modelling with adaptively refined finite volume methods, Acta Numerica, 20, 211, https://doi.org/10.1017/S0962492911000043, 2011.

Liang, D., Gotoh, H., Khayyer, A., and Chen, J. M.: Boussinesq modelling of solitary wave and N-wave runup on coast, Applied ocean research, 42, 144–154, 2013.

Lo, H.-Y., Park, Y. S., and Liu, P. L.-F.: On the run-up and back-wash processes of single and double solitary waves — An experimental study, Coastal Engineering, 80, 1–14, https://doi.org/https://doi.org/10.1016/j.coastaleng.2013.05.001, 2013.

Løvholt, F., Harbitz, C. B., and Haugen, K. B.: A parametric study of tsunamis generated by submarine slides in the Ormen Lange/Storegga area off western Norway, in: Ormen Lange–an Integrated Study for Safe Field Development in the Storegga Submarine Area, pp. 219–231, Elsevier, https://doi.org/10.1016/j.marpetgeo.2004.10.017, 2005.

Løvholt, F., Pedersen, G., Harbitz, C. B., Glimsdal, S., and Kim, J.: On the characteristics of landslide tsunamis, Philosophical Transactions of the Royal Society A: Mathematical, Physical and Engineering Sciences, 373, 20140 376, https://doi.org/10.1098/rsta.2014.0376, 2015.

Lynett, P. J.: Tsunami Inundation, Modeling of, pp. 117–133, Springer US, New York, NY, ISBN 978-1-0716-1705-2, https://doi.org/10.1007/978-1-0716-1705-2_569, 2022.

https://doi.org/10.5194/egusphere-2026-2890
Preprint. Discussion started: 16 July 2026


Madsen, P. A. and Schaeffer, H. A.: Analytical solutions for tsunami runup on a plane beach: single waves, N-waves and transient waves, Journal of Fluid Mechanics, 645, 27–57, 2010.

Madsen, P. A. and Sørensen, O. R.: A new form of the Boussinesq equations with improved linear dispersion characteristics. Part 2. A slowly-varying bathymetry, Coastal engineering, 18, 183–204, https://doi.org/10.1016/0378-3839(92)90019-Q, 1992.

Madsen, P. A., Murray, R., and Sørensen, O. R.: A new form of the Boussinesq equations with improved linear dispersion characteristics, Coastal engineering, 15, 371–388, https://doi.org/10.1016/0378-3839(91)90017-B, 1991.

Madsen, P. A., Fuhrman, D. R., and Schäffer, H. A.: On the solitary wave paradigm for tsunamis, Journal of Geophysical Research: Oceans, 113, 2008a.

Madsen, P. A., Fuhrman, D. R., and Schäffer, H. A.: On the solitary wave paradigm for tsunamis, Journal of Geophysical Research: Oceans, 113, https://doi.org/10.1029/2008JC004932, 2008b.

McColl, S. T.: Paraglacial rock-slope stability, Geomorphology, 153, 1–16, 2012.

Miller, D. J.: The Alaska earthquake of July 10, 1958: giant wave in Lituya Bay, Bulletin of the Seismological Society of America, 50, 253–266, 1960.

Montoya, L. H. and Lynett, P.: Quantifying numerical model accuracy and variability, Coastal Engineering Proceedings, pp. 12–12, https://doi.org/10.9753/icce.v35.currents.12, 2016.

Nigg, V., Bacigaluppi, P., Vetsch, D. F., Vogel, H., Kremer, K., and Anselmetti, F. S.: Shallow-water tsunami deposits: evidence from sediment cores and numerical wave propagation of the 1601 CE Lake Lucerne event, Geochemistry, Geophysics, Geosystems, 22, e2021GC009 753, 2021.

Nwogu, O.: Alternative form of Boussinesq equations for nearshore wave propagation, Journal of waterway, port, coastal, and ocean engineering, 119, 618–638, https://doi.org/10.1061/(ASCE)0733-950X(1993)119:6(618), 1993.

Patton, A., Rathburn, S., Capps, D., McGrath, D., and Brown, R.: Ongoing landslide deformation in thawing permafrost, Geophysical research letters, 48, e2021GL092 959, 2021.

Peregrine, D. H.: Long waves on a beach, Journal of fluid mechanics, 27, 815–827, https://doi.org/10.1017/S0022112067002605, 1967.

Qu, K., Ren, X., and Kraatz, S.: Numerical investigation of tsunami-like wave hydrodynamic characteristics and its comparison with solitary wave, Applied Ocean Research, 63, 36–48, https://doi.org/https://doi.org/10.1016/j.apor.2017.01.003, 2017.

Rafliana, I., Jalayer, F., Cerase, A., Cugliari, L., Baiguera, M., Salmanidou, D., Necmioğlu, Ö., Ayerbe, I. A., Lorito, S., Fraser, S., et al.: Tsunami risk communication and management: Contemporary gaps and challenges, International Journal of Disaster Risk Reduction, 70, 102 771, 2022.

Roberts, N. J., McKillop, R. J., Lawrence, M. S., Psutka, J. F., Clague, J. J., Brideau, M.-A., and Ward, B. C.: Impacts of the 2007 Landslide-Generated Tsunami in Chehalis Lake, Canada, pp. 133–140, Springer Berlin Heidelberg, Berlin, Heidelberg, https://doi.org/10.1007/978-3-642-31319-6_19, 2013.

Ruffini, G., Heller, V., and Briganti, R.: Numerical modelling of landslide-tsunami propagation in a wide range of idealised water body geometries, Coastal Engineering, 153, 103 518, 2019.

Schäffer, H. A. and Madsen, P. A.: Further enhancements of Boussinesq-type equations, Coastal Engineering, 26, 1–14, https://doi.org/10.1016/0378-3839(95)00017-2, 1995.

Schnellmann, M., Anselmetti, F. S., Giardini, D., McKenzie, J. A., and Ward, S. N.: Prehistoric earthquake history revealed by lacustrine slump deposits, Geology, 30, 1131–1134, 2002.

https://doi.org/10.5194/egusphere-2026-2890
Preprint. Discussion started: 16 July 2026


Segur, H.: The Korteweg-de Vries equation and water waves. Solutions of the equation. Part 1, Journal of Fluid Mechanics, 59, 721–736, 1973.

Siegenthaler, C. and Sturm, M.: Slump induced surges and sediment transport in Lake Uri, Switzerland, Internationale Vereinigung für theoretische und angewandte Limnologie: Verhandlungen, 24, 955–958, 1991.

St-Germain, P., Nistor, I., Readshaw, J., and Lamont, G.: NUMERICAL MODELING OF COASTAL DIKE OVERTOPPING USING SPH AND NON-HYDROSTATIC NLSW EQUATIONS$_2014, Coastal Engineering Proceedings, 1,$ https://doi.org/10.9753/$icce.v34.structures.10, 2014.$

Strasser, M., Hilbe, M., and Anselmetti, F. S.: Mapping basin-wide subaquatic slope failure susceptibility as a tool to assess regional seismic and tsunami hazards, Marine Geophysical Research, 32, 331–347, https://doi.org/10.1007/s11001-010-9100-2, 2011.

Strupler, M., Hilbe, M., Anselmetti, F. S., Kopf, A. J., Fleischmann, T., and Strasser, M.: Probabilistic stability evaluation and seismic triggering scenarios of submerged slopes in Lake Zurich (Switzerland), Geo-Marine Letters, 37, 241–258, https://doi.org/10.1007/s00367-017-0492-8, 2017.

Strupler, M., Hilbe, M., Kremer, K., Danciu, L., Anselmetti, F. S., Strasser, M., and Wiemer, S.: Subaqueous landslide-triggered tsunami hazard for Lake Zurich, Switzerland, Swiss journal of geosciences, 111, 353–371, https://doi.org/10.1007/s00015-018-0308-5, 2018.

Strupler, M., Bacigaluppi, P., Kremer, K., Vetsch, D., Anselmetti, F. S., Robert, B., and Wiemer, S.: Abschätzung der Gefährdung durch Tsunamis in perialpinen Seen infolge Unterwasserhangrutschungen, vol. 112, pp. 11–16, Baden: SWV, 2020a.

Strupler, M., Evers, F. M., Kremer, K., Cauzzi, C., Bacigaluppi, P., Vetsch, D. F., Boes, R. M., Fäh, D., Anselmetti, F. S., and Wiemer, S.: A simplified classification of the relative tsunami potential in Swiss perialpine lakes caused by subaqueous and subaerial mass-movements, Frontiers in Earth Science, 8, 564 783, 2020b.

Svennevig, K., Hicks, S. P., Forbriger, T., Lecocq, T., Widmer-Schnidrig, R., Mangeney, A., Hibert, C., Korsgaard, N. J., Lucas, A., Satriano, C., Anthony, R. E., Mordret, A., Schippkus, S., Rysgaard, S., Boone, W., Gibbons, S. J., Cook, K. L., Glimsdal, S., Løvholt, F., Noten, K. V., Assink, J. D., Marboeuf, A., Lomax, A., Vanneste, K., Taira, T., Spagnolo, M., Plaen, R. D., Koelemeijer, P., Ebeling, C., Cannata, A., Harcourt, W. D., Cornwell, D. G., Caudron, C., Poli, P., Bernard, P., Larose, E., Stutzmann, E., Voss, P. H., Lund, B., Cannavo, F., Castro-Díaz, M. J., Chaves, E., Dahl-Jensen, T., Dias, N. D. P., Déprez, A., Develter, R., Dreger, D., Evers, L. G., Fernández-Nieto, E. D., Ferreira, A. M. G., Funning, G., Gabriel, A.-A., Hendrickx, M., Kafka, A. L., Keiding, M., Kerby, J., Khan, S. A., Dideriksen, A. K., Lamb, O. D., Larsen, T. B., Lipovsky, B., Magdalena, I., Malet, J.-P., Myrup, M., Rivera, L., Ruiz-Castillo, E., Wetter, S., and Wirtz, B.: A rockslide-generated tsunami in a Greenland fjord rang Earth for 9 days, Science, 385, 1196–1205, https://doi.org/10.1126/science.adm9247, 2024.

Svennevig, K., Keiding, M., Sørensen, E. V., Løvholt, F., Glimsdal, S., Perez, L. F., Owen, M. J., and Morino, C.: Two similar permafrost degradation landslides at Paatuut, West Greenland, caused tsunamis of substantially different magnitudes, Landslides, 22, 1455–1474, 2025.

Synolakis, C. E., Bardet, J.-P., Borrero, J. C., Davies, H. L., Okal, E. A., Silver, E. A., Sweet, S., and Tappin, D. R.: The slump origin of the 1998 Papua New Guinea tsunami, Proceedings of the Royal Society of London. Series A: Mathematical, Physical and Engineering Sciences, 458, 763–789, https://doi.org/10.1098/rspa.2001.0915, 2002.

Tadepalli, S. and Synolakis, C. E.: The run-up of N-waves on sloping beaches, Proceedings of the Royal Society of London. Series A: Mathematical and Physical Sciences, 445, 99–112, 1994.

Tappin, D. R.: The generation of tsunamis, Encyclopedia of maritime and offshore engineering, pp. 1–10, https://doi.org/10.1002/9781118476406.emoe523, 2017.

Team, C. D.: CLAWPACK software, http://www.clawpack.org.

Toro, E. F., Spruce, M., and Speares, W.: Restoration of the contact surface in the HLL-Riemann solver, Shock waves, 4, 25–34, https://doi.org/10.1007/BF01414629, 1994.

https://doi.org/10.5194/egusphere-2026-2890
Preprint. Discussion started: 16 July 2026


Vetsch, D., Siviglia, A., Bacigaluppi, P., Bürgler, M., Caponi, F., Conde, D., Gerke, E., Kammerer, S., Koch, A., Peter, S., Vanzo, D., Vonwiller, L., and Weberndorfer, M.: System Manuals of BASEMENT, Version 3.0., laboratory of Hydraulics, Glaciology and Hydrology (VAW). ETH Zurich. Available from https://www.basement.ethz.ch, 2019.

Wang, J., Ward, S. N., and Xiao, L.: Numerical simulation of the December 4, 2007 landslide-generated tsunami in Chehalis Lake, Canada, Geophysical Journal International, 201, 372–376, 2015.

Watts, P., Grilli, S. T., Tappin, D. R., and Fryer, G. J.: Tsunami Generation by Submarine Mass Failure. II: Predictive Equations and Case Studies, Journal of Waterway, Port, Coastal, and Ocean Engineering, 131, 298–310, https://doi.org/10.1061/(ASCE)0733-950X(2005)131:6(298), 2005.

Wolken, G. J., Liljedahl, A. K., Brubaker, M., Coe, J. A., Fiske, G., Christiansen, H. H., Jacquemart, M., Jones, B. M., Kääb, A., Løvholt, F., et al.: Glacier and permafrost hazards, Arctic report card, 2021.

Yeh, H., Liu, P., Briggs, M., and Synolakis, C.: Propagation and amplification of tsunamis at coastal boundaries, Nature, 372, 353–355, 1994.

Yu, G., Yu, B., Sun, S., and Tao, W.-Q.: Comparative Study on Triangular and Quadrilateral Meshes by a Finite-Volume Method with a Central Difference Scheme, Numerical Heat Transfer, Part B: Fundamentals, 62, 243–263, https://doi.org/10.1080/10407790.2012.709416, 2012.